J. Appl. Comput. Mech., xx(x) (2026) 1-17
DOI: 10.22055/jacm.2026.49538.6058

ISSN: 2383-4536
jacm.scu.ac.ir

Shahid Chamran University of Ahvaz

Journal of Applied and Computational Mechanics



Research Paper

Numerical Study of Heat Recirculation on Combustion Performance and Thermal Efficiency in a Novel Hydrogen–Air Micro-Combustor

Mohammad Ali Attarian, Alireza Alipoor

School of Mechanical Engineering, Shiraz University, Shiraz, 71348-51154, Iran,
Email: ali.attarianshiraz@gmail.com (M.A.A.); a.alipoor@shirazu.ac.ir (A.A.)

Received July 07 2026; Revised September 17 2026; Accepted for publication October 11 2026.
✉ Corresponding author: A. Alipoor (a.alipoor@shirazu.ac.ir)
© 2026 Published by Shahid Chamran University of Ahvaz

Abstract. Micro-scale combustion systems integrated with hydrogen fuel and thermophotovoltaic (TPV) technology provide a promising solution for compact and efficient power generation. In this study, premixed hydrogen–air combustion is numerically investigated in an MIT-inspired micro gas turbine combustion chamber featuring combined curvature, expansion, and contraction, enabling enhanced flame stabilization and reactant preheating. A three-dimensional numerical model is developed to analyze the influence of inlet flow velocity, equivalence ratio, and wall thermal conductivity on combustion behavior and system performance. The results show that increasing inlet velocity from 4 m/s to 8 m/s reduces thermal efficiency from 12.27% to 10.56% due to shorter residence time. Higher velocities also shift the flame downstream and increase peak OH concentration, indicating intensified but less complete reactions. Variations in equivalence ratio reveal that maximum temperature and OH mass fraction increase as the mixture approaches stoichiometric conditions, reaching peak values of 1934 K and 0.0102 at $\varphi = 1$, and then decrease under rich conditions due to oxygen limitation. In addition, the flame location shifts significantly toward the inlet as φ increases. Thermal conductivity demonstrates a competing effect: increasing conductivity from 1.4 to 6.7 W/m·K improves efficiency (up to 9.05%) and enhances temperature uniformity through better heat redistribution, while further increases to 12.63 W/m·K reduce peak solid temperature and slightly decrease efficiency due to excessive heat loss. Higher conductivity also shifts the flame upstream and increases OH concentration by strengthening preheating and reaction rates.

Keywords: Hydrogen, Novel micro combustor, Radiative efficiency, Micro-thermophotovoltaic system.

1. Introduction

Microscale combustion technology has attracted growing interest in recent years due to its ability to generate power from various fuels in compact systems for applications such as satellites, micro-robots, and portable electronics. Compared with lithium-ion batteries [1–3], micro-combustors provide higher energy density and greater flexibility. However, flame stability is difficult to maintain because the high surface-to-volume ratio increases heat losses and promotes quenching. Various strategies, including geometric optimization, preheating, and flame stabilization methods, have been proposed to improve combustion performance [4].

Alipoor and Saidi [5] examined a premixed hydrogen–air micro-combustor with a single U-shaped channel and showed that enhanced preheating in the curved geometry increases flammability limits by at least fourfold compared to straight channels. It was further found that efficiency declines as inlet velocity increases, and attains a maximum value at a wall thermal conductivity of 3 $W{\cdot}m^{-1}{\cdot}K^{-1}$. Yang et al. [6] studied the effects of channel wall thermal conductivity and diameter on the combustion and thermal behavior of a premixed hydrogen–air flame in a micro chamber. They reported that higher thermal conductivity increases the outer wall temperature near the inlet, improving temperature uniformity. Increasing thermal conductivity from 0.1 to 10 $W{\cdot}m^{-1}{\cdot}K^{-1}$ reduced wall temperature deviation from 292.8 K to 47.9 K, thereby enhancing combustion efficiency and uniformity. Yang et al. [7] explored interplay between equivalence ratio, inlet velocity, wall material, and the effect of recirculation zones within a cylindrical combustion chamber. This chamber featured an annular inlet equipped with six straight vanes, angled at 45 degrees, designed to induce swirling flow and enhance flame stability in premixed hydrogen–air mixtures. Their findings revealed that the inner recirculation zone serves as the primary mechanism for flame stabilization.

Zhang et al. [8] studied bluff bodies and fins in a stepped micro-combustor and found that triangular bluff bodies combined with steps improve efficiency more than fins, by about 10.8%, while fins with steps most strongly increase the Damköhler number.

Published online: November 26 2026

Fontana et al. [9] investigated a straight microtube with two triangular obstacles for heat recirculation and reported thermal efficiency improvements of up to 15% and 40% at inlet velocities of 0.4 and 0.6 m/s, respectively.

Abbaspour and Alipoor [10] showed that a convergent–divergent micro-combustor improves flame stability at higher inlet velocities and exhibits oscillatory behavior at 8 m/s, a 3.45° throat angle, and φ = 0.5–0.8. Naeimi and Hashemi [11] examined the impact of equivalence ratio, wall thickness, wall thermal properties, and chamber geometry on the critical inlet velocity and blow-off limit. Their findings indicated that an elevated equivalence ratio enhances the maximum achievable inlet velocity, thereby promoting a stable flame. Furthermore, they observed that a thicker wall contributed to increased flame stability.

Gao et al. [12] studied inlet velocity (8–40 m/s), wall materials (quartz, steel, silicon carbide), and equivalence ratio (0.6–1.4) in micro thermophotovoltaic combustion. They found reduced wall heat losses and improved efficiency compared with conventional chambers. At 40 m/s, wall heat loss decreased by 15.9%, reaction power increased by 17.5%, and combustion efficiency rose by 5.9%.

The numerical study by Rezende et al. [13] examined a stoichiometric premixed hydrogen–air mixture in a wavy micro-channel and found that the wavy configuration enhances flame–wall interaction, leading to increased heat transfer and improved temperature uniformity. Gao et al. [14] showed that adding vanes at step edges enhances preheating and flame stability, expanding blow-off limits from 3–33 m/s to 14–121.5 m/s.

You et al. [15] showed that fins reduce temperature uniformity by ~17% at 4 m/s, while increasing velocity from 4 to 7 m/s improves uniformity by 42% without fins and 37% with fins. Tang et al. [16] reported that a multi-cavity micro-combustor reaches its highest wall temperature at φ = 0.9 and U = 3 m/s. Huang et al. [17] experimentally and numerically studied the influence of multiple bluff bodies on the combustion behavior of H_2/CH_4/air mixtures, considering parameters such as number, placement, and width of the bluff bodies. They found that an optimal radiative efficiency of 27% can be achieved, significantly exceeding that of configurations without bluff bodies. In another study, Abbaspour and Alipoor [18] investigated a wavy micro-combustor aimed at improving flammability limits and thermal efficiency. Their results indicated that, for equivalence ratios between 0.4 and 0.6, the upper flammability limit increases by a factor of three compared with flat-wall designs, with efficiency improvements reaching up to 8.89%. Sadeghi et al. [19] experimentally examined methane–oxygen flames over an equivalence ratio range of 1.5 to 3.38, reporting optimal stability between 1.94 and 2.26, and flame extinction at Reynolds numbers above 2754. These findings highlight key developments in micro-combustor research.

The study by Zuo et al. [20] examined hydrogen combustion in a micro-combustor featuring two symmetric cylindrical outlet tubes, focusing on the effects of inlet velocity, equivalence ratio, and outlet geometry on pressure drop and thermal efficiency. They reported that pressure drop increases with inlet velocity, while thermal efficiency is maximized at intermediate flow velocities. No noticeable effect of equivalence ratio on pressure drop was observed, and peak efficiency occurred at stoichiometric conditions (φ = 1). Furthermore, larger outlet tube diameters were found to reduce pressure losses, whereas longer tubes provided a slight improvement in thermal efficiency. In another study, Zuo et al. [21] investigated a hydrogen-fueled micro-combustor in three configurations: without a baffle body, with a simple baffle body, and with a finned baffle body. The aim was to have a uniform temperature distribution and improve efficiency. The results showed that the micro-combustor with a finned baffle showed the highest and most uniform wall temperature, although its pressure drop was higher than in the other configurations. Furthermore, to determine the optimal configuration, fin angles of 30°, 45°, 60°, 75°, and 90° were examined, with the 60° angle yielding the best overall performance.

Dai et al. [22] examined micro-combustion chambers incorporating multi-layer bluff bodies with the objective of enhancing energy efficiency. Their findings indicated that extending the bluff body length, while resulting in a higher pressure drop, elevated the wall temperature and improved overall system efficiency. Moreover, for a fixed bluff body length, increasing the number of bluff bodies led to higher combustion chamber temperatures without inducing an additional pressure drop. Dai et al. [23] further examined the influence of V-shaped baffles on combustion behavior, analyzing angles between 90° and 120° with 15° increments. Their results indicated that reducing the baffle angle from 120° to 90° lowers pressure losses and improves temperature uniformity, with negligible effect on energy efficiency. Moreover, increasing the baffle height was found to increase pressure drop while simultaneously raising the maximum outer wall temperature and enhancing temperature uniformity. They also observed that the distance between the baffle and inlet has a negligible effect on both energy efficiency and pressure drop. A regenerative-type micro-combustor with a dual reaction zone was proposed by Tenkolu et al. [24]. The design incorporates three internal barriers to divide the combustor and promote heat recirculation. Their findings indicated that, at a barrier length of 50 mm, the flame length reached 38.6 mm, the wall temperature variation was limited to a standard deviation of 30 K, and the radiative energy output achieved 80 W.

Heat recirculation has been recognized as an effective strategy for overcoming the heat-loss and flame-stabilization challenges associated with microscale combustion. Early studies demonstrated that heat-recirculating configurations can recover thermal energy from the hot combustion products and transfer it to the incoming reactants, thereby enhancing reactant preheating and extending the stable combustion regime [25, 26]. Subsequent studies further developed heat-recirculating and Swiss-roll-type micro-combustors and demonstrated the importance of internal recirculation, channel arrangement, and geometric heat transfer in improving flame stability and thermal performance [27, 28]. More recent investigations have continued to explore the thermal and combustion characteristics of heat-recirculating micro-combustors under different geometric and operating conditions [29-32]. In parallel with heat-recirculating configurations, radial micro-combustors have attracted considerable attention because their flow arrangement can provide compact geometries and effective flame stabilization through the interaction between radial flow, heat recirculation, and wall heat transfer [25, 26, 32]. These studies have demonstrated that geometric configuration plays a critical role in controlling the flow field, flame location, thermal distribution, and overall combustion performance of microscale combustors.

This work aims to numerically investigate the combustion characteristics of hydrogen–air mixtures in a microscale combustion chamber based on an MIT-inspired micro gas turbine configuration [2, 3, 8, 9]. Unlike several previously reported heat-recirculation micro-combustors that employ discrete geometric features, such as steps, fins, or bluff bodies, to promote flow recirculation and flame stabilization, the present configuration integrates continuous curvature with expansion and contraction within a single compact flow passage. The combined geometry promotes internal flow recirculation and heat transfer from the hot downstream region toward the incoming reactants, thereby enhancing reactant preheating and flame stabilization without relying on multiple internal flame-holding obstacles. Thus, the novelty of the present configuration lies not in the individual use of curvature, expansion, or contraction, but in their integrated arrangement within a compact micro-combustor and their combined role in establishing heat recirculation and controlling the combustion characteristics. At the same time, this configuration can mitigate

some limitations associated with discrete flame-holding elements, including increased pressure drop, flow obstruction, and geometric complexity, while maintaining a compact architecture suitable for microscale applications.

Beyond its combustion and heat-recirculation characteristics, the proposed flow configuration offers potential for integration with rotating energy-conversion components, such as a turbine and compressor. Such integration could enable the system to exploit two complementary energy-conversion pathways: electrical power generation through thermophotovoltaic (TPV) cells receiving thermal radiation from the hot combustion region, and mechanical power generation through the rotating turbine–compressor unit. This feature provides the potential to develop a compact integrated micro power-generation system capable of simultaneously utilizing the radiative and mechanical energy associated with the combustion process. Accordingly, the proposed configuration provides a promising platform not only for heat-recirculation-assisted combustion but also for the development of compact hybrid micro power-generation systems.

In addition to evaluating the geometric and energy-conversion potential of the proposed configuration, this work conducts a comprehensive three-dimensional numerical investigation of the principal operating and physical parameters governing its combustion characteristics. In particular, the coupled effects of equivalence ratio, inlet flow velocity, and wall thermal conductivity are systematically examined. Although these parameters individually play important roles in determining flame stability, heat transfer, reaction rates, and overall system performance, their combined effects within complex micro-combustor geometries have not yet been fully elucidated. The present study therefore quantifies their effects on temperature distribution, flame position, radical species formation, thermal efficiency, and power output, with particular emphasis on identifying the interactions between operating conditions and wall thermal properties. By combining an integrated heat-recirculation geometry with a systematic parametric investigation, this study aims to improve the understanding of microscale combustion behavior and identify operating conditions that enhance both combustion stability and energy-conversion performance.

2. Numerical Approach

This section introduces the governing equations and physical parameters of the numerical model, followed by the combustor geometry, solution methodology, and boundary conditions. The model is then validated using available data to ensure accuracy and reliability.

2.1. Governing equations

The numerical simulations were performed assuming steady, premixed combustion of an ideal-gas hydrogen–air mixture. The mixture was considered fully homogeneous before entering the combustor. The governing equations for conservation of mass, momentum, energy, and species are presented in Eqs. (1) to (4).

- Continuity:

$$\nabla.(\rho\mathbf{u}) = 0 \tag{1}$$

- Momentum:

$$\begin{aligned} \rho(\mathbf{u}.\nabla\mathbf{u}) &= -\nabla p + \nabla.(\mu\mathbf{S}) \\ \mathbf{S} &= \nabla\mathbf{u} + (\nabla\mathbf{u})^{\boldsymbol{T}} - \frac{\mathbf{2}}{\mathbf{3}}(\nabla.\mathbf{u})\mathbf{I} \end{aligned} \tag{2}$$

For the momentum equation, $\mathbf{u}$, ρ and μ denote velocity vector, density and dynamic viscosity, while $\mathbf{S}$, $\mathbf{I}$, and p represent the stress tensor, identity matrix and, pressure, respectively.

- Energy:

$$\begin{aligned} \rho c_p(\mathbf{u}.\nabla T) &= \nabla.(\lambda\nabla T) - \sum_{i=1}^{N} h_i\dot{\omega}_i - \rho\left(\sum_{i=1}^{N} C_{p,i}Y_i\mathbf{V}_i\right).\nabla T \\ \mathbf{V}_i &= -\left(\frac{D_{im}}{X_i}\right)\nabla X_i \end{aligned} \tag{3}$$

In the energy equation, Y_i, $\dot{\omega}_i$, λ, $\mathbf{V}_i$, and h_i correspond to species mass fraction, reaction rate, thermal conductivity, diffusion velocity, and species enthalpy, respectively. Species transport is governed by Eq. (4):

$$\rho(\mathbf{u}.\nabla Y_i) = -\nabla.(\rho Y_i\mathbf{V}_i) + \dot{\omega}_i \qquad i = 1,\ldots,N \tag{4}$$

The density can be calculated using the ideal gas equation of state. The energy equation in a solid zone is expressed as:

$$\nabla.(\lambda_s\nabla T) = 0 \tag{5}$$

where λ_s is solid thermal conductivity.

The laminar finite-rate approach is used to calculate Arrhenius-based reaction rates. Fluid properties, including specific heat, thermal conductivity, and viscosity, are assumed to vary with temperature and mixture composition.

The present study also examines thermophotovoltaic power-generation performance through three thermal efficiency parameters. The energy conversion efficiency (η_Q) is defined as the ratio of total wall heat transfer, including convection and radiation, to the chemical heat release rate:

$$\eta_Q = \frac{\dot{Q}_{wall}}{\dot{Q}_R} \tag{6}$$

where $\dot{Q}_{wall}$ and $\dot{Q}_R$ represent the heat transfer rate from the external walls and the chemical heat release rate, respectively. The total heat transfer rate from the external walls is calculated by integrating the combined convective and radiative heat fluxes over the entire external wall surface:

$$\dot{Q}_{\text{wall}} = \int_{A_{\text{ext}}} [h(T_s - T_\infty) + \varepsilon\sigma(T_s^4 - T_{\text{sur}}^4)]\, dA \tag{7}$$

where A is the external wall surface area, h is the convective heat-transfer coefficient, T_s is the external wall surface temperature, T_∞ is the ambient temperature, ε is the wall emissivity, and σ is the Stefan–Boltzmann constant:

$$\dot{Q}_R = \dot{m}_{h_2} Q_{LHV} \tag{8}$$

where $\dot{m}_{H_2}$ is the hydrogen mass flow rate, and QLHV is the lower heating value of hydrogen 119 MJ/kg [5].

The emitter efficiency, η_{Rad}, is defined as the ratio of radiative heat transfer from the combustor outer surfaces ($\dot{Q}_{Rad}$) to the chemical heat release rate ($\dot{Q}_R$):

$$\eta_{Rad} = \frac{\dot{Q}_{Rad}}{\dot{Q}_R} \tag{9}$$

$$\dot{Q}_{Rad} = \sigma\varepsilon(T_s^4 - T_{sur}^4) \tag{10}$$

The overall efficiency of energy conversion in TPV systems ($\dot{\eta}_{total}$) can be calculated by multiplying the emitter efficiency ($\dot{\eta}_{Rad}$) in the efficiency of the TPV array ($\dot{\eta}_{TPV}$):

$$\eta_{total} = \eta_{Rad}\eta_{TPV} \tag{11}$$

The TPV array efficiency, η_{TPV}, represents the conversion of incident radiative thermal energy into electrical power. In the present study, a constant TPV conversion efficiency of 20% is assumed based on representative values reported in previous studies [18, 33–37]. This value is adopted as a system-level reference efficiency to estimate the potential electrical power output associated with the radiative energy supplied by the micro-combustor. The assumed value does not represent the experimentally measured efficiency of a specific TPV cell. Rather, it provides a consistent conversion factor for evaluating the relative effects of combustor operating conditions and radiative thermal performance on the potential electrical output. The actual TPV efficiency depends on the spectral characteristics and temperature of the radiative source, cell bandgap, spectral matching, and wavelength-dependent photovoltaic response.

A premixed hydrogen–air mixture enters the micro-combustor at a prescribed inlet velocity and equivalence ratio, with an inlet temperature of 300 K. The inlet velocity and equivalence ratio are varied according to the investigated operating conditions, while the inlet temperature is maintained at 300 K. Velocity, temperature, and species mass fractions are prescribed at the inlet, while pressure is assigned a zero-gradient condition. The inner walls satisfy the no-slip condition, and conjugate heat transfer is applied at the fluid–solid interface. Convective and radiative heat losses are considered at the combustor walls with ambient temperature, emissivity, and convection coefficient fixed at 300 K, 0.93, and 20 W/m²·K, respectively. Quartz, titanium, and steel walls with thermal conductivities of 1.4, 6.7 and 12.63 W/m·K [34] are considered. The outlet pressure is set to 1 atm, and the initial domain temperature is 1900 K. The initial temperature of the computational domain was set to 1900 K to provide sufficient initial thermal energy for initiating the combustion reaction and to facilitate convergence of the steady-state reacting-flow solution. This value represents only a numerical initialization condition and does not correspond to the actual operating temperature of the combustor. The hydrogen–air mechanism includes nine species and 23 reversible reactions [38].

Because of the small hydraulic diameter of the microchannels, the flow regime and the applicability of the standard k-εmodel require clarification. Using the properties of the premixed H_2/air mixture at 300 K and 1 atm, the inlet Reynolds number ranges from approximately 500 to 2000 over the investigated inlet velocity (4–16 m/s) and equivalence-ratio conditions. Thus, according to the conventional criterion for internal flow in straight channels, the inlet flow remains within the laminar regime. Nevertheless, the present combustor contains strongly curved three-dimensional passages, and the inlet Reynolds number alone does not completely characterize the internal transport processes. Kuo and Ronney [39] showed that, in non-adiabatic heat-recirculating Swiss-roll combustors, turbulent transport became important for reproducing experimentally observed extinction behavior at Reynolds numbers above approximately 500. Moreover, Chen and Ronney [40] demonstrated that three-dimensional Swiss-roll channels can develop Dean-type secondary vortices even without a turbulence model, producing transverse heat transport comparable to that obtained with turbulent transport.

The use of turbulence formulations has also been reported in subsequent three-dimensional micro-combustor studies. Fan et al. [41] employed a three-dimensional steady-state $k-\varepsilon$ model for a microscale Swiss-roll combustor with a bluff body. Similarly, Zuo et al. [42] used the standard $k-\varepsilon$ model for a hydrogen-fueled counter-flow double-channel micro-combustor. In addition, Yılmaz et al. [43] evaluated several turbulence formulations, including the standard, RNG, and realizable $k-\varepsilon$ models, for H_2/air combustion in a micro-cylindrical combustor.

Based on these considerations, the standard $k-\varepsilon$ model was used in the present study as a modeling approximation for the three-dimensional curved reacting flow. The selected model is therefore intended to account for the complex transport associated with the curved three-dimensional geometry and the resulting secondary-flow and recirculation effects.

The numerical simulations were carried out using ANSYS Fluent 2022 R1 under a three-dimensional steady-state formulation. Pressure–velocity coupling was solved using the Coupled algorithm. Second-order upwind spatial discretization schemes were used for the pressure, momentum, energy, and species transport equations, whereas first-order upwind schemes were adopted for the turbulent kinetic energy (k), turbulent dissipation rate (ε), and radiation transport equations. Radiative heat transfer was modeled using the Discrete Ordinates (DO) radiation model. As the simulations were performed under steady-state conditions, no temporal discretization scheme was applied. The convergence criterion for all residuals was set to 10^{-6}.

To quantitatively evaluate the spatial temperature distribution, the average temperature and standard deviation were calculated over the specified computational region. For a region containing N computational cells, the average temperature is defined as:

$$T = \frac{1}{N}\sum_{i=1}^{N} T_i \tag{12}$$



where T_i denotes the temperature of the i-th computational cell. The standard deviation of the temperature distribution is then calculated as:

$$\sigma_T = \sqrt{\frac{1}{N}\sum_{i=1}^{N}(T_i - T)^2} \tag{13}$$

The temperature uniformity index is defined as:

$$\mathrm{TU} = 1 - \frac{\sigma_T}{T} \tag{14}$$

A higher value of TU represents a more uniform temperature distribution, while a lower value indicates greater spatial temperature variation. These quantities are calculated from all computational cells within the specified evaluation region and are used to quantify the temperature distributions.

2.2. Geometry

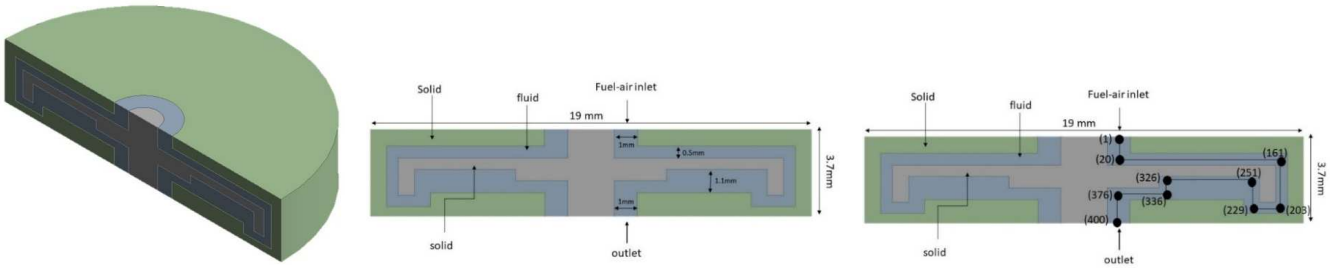
Figure 1(a) illustrates the schematic of the combustion chamber geometry, which is based on an MIT micro-combustor design [2, 3, 8, 9]. The geometry consists of a disk-shaped chamber with a diameter of 19 mm and a height of 3.7 mm. The reactant mixture enters axially, passes through the gray-colored region, and exits at the downstream boundary. The two-dimensional mid-plane of the combustor is shown in Fig. 1(b), where the inlet and outlet positions, flow passage, and geometric parameters are indicated. Both inlet and outlet widths are 1 mm, while the channel height varies from 0.5 mm at the inlet region to 1.1 mm downstream. For post-processing, the line shown in Fig. 1(c) is defined as the flow centerline. A total of 400 uniformly distributed points is defined along this line, with point 1 corresponding to the inlet and point 400 to the outlet. The indices indicating flow-direction changes are also specified.

2.3. Validation of the numerical simulation and grid study

The numerical model is validated against Wan et al. [44], who studied lean hydrogen–air combustion in a bluff-body micro-channel and evaluated the effects of inlet velocity and equivalence ratio on blow-off limits, efficiency, and exhaust temperature. Their results show that the bluff body significantly increases the blow-off limit, which further rises as the equivalence ratio increases from 0.4 to 0.6. Combustion efficiency and exhaust temperature first increase with inlet velocity and then decrease.

Figure 2 compares the exhaust gas temperature variation with inlet velocity between the present numerical results and the experimental data reported by Wan et al. [44]. The comparison is performed for an equivalence ratio of 0.5, inlet velocities between 3 and 35 m/s, and a quartz combustor wall. The results demonstrate strong agreement between simulations and experiments, indicating that the numerical model accurately predicts the exhaust gas temperature over the full range of inlet velocities.

To ensure mesh independence, the geometry in Fig. 1 was discretized using several grid resolutions. Meshes containing 150,000, 350,000, 550,000, 750,000, and 850,000 elements were tested at an inlet velocity of 8 m/s, an equivalence ratio of 0.5, and a thermal conductivity of 1.4 W/m·K. The resulting temperature and OH mass fraction distributions along the flow centerline are presented in Fig. 3, indicating that the solution becomes grid independent as mesh density increases. Accordingly, a mesh with 750,000 elements was adopted for the present work.



(a) (b) (c)

Fig. 1. Schematic of the geometry of the micro combustion chamber in (a) three-dimensional, (b) two dimensional, in the cross-sectional plane, (c) Centerline flow path.

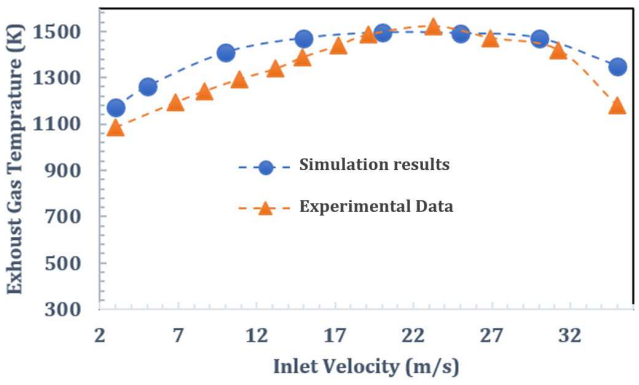


Fig. 2. Comparison of the present numerical results with the experimental data reported by Wan et al. [44], effect of inlet velocity on exhaust gas temperature at φ = 0.5.

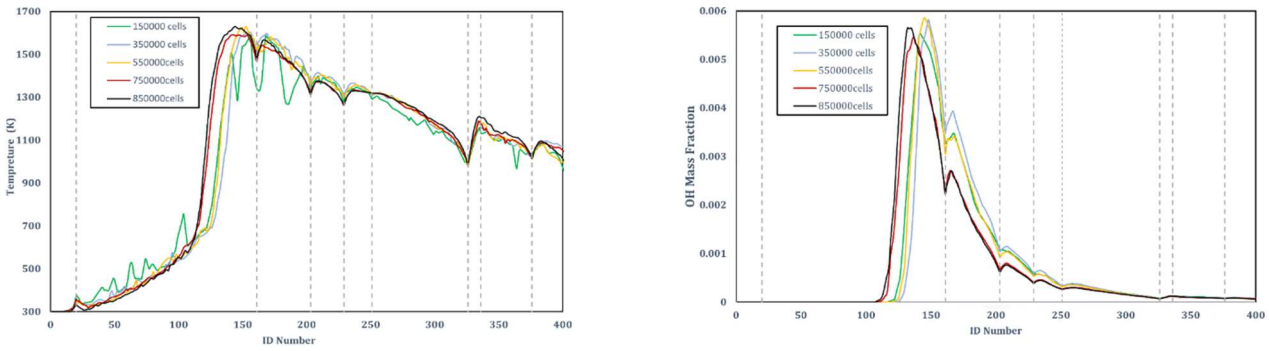


Fig. 3. Diagram of temperature changes and mass fraction of OH species in the combustion chamber in terms of the number of points on the center line for different grids.

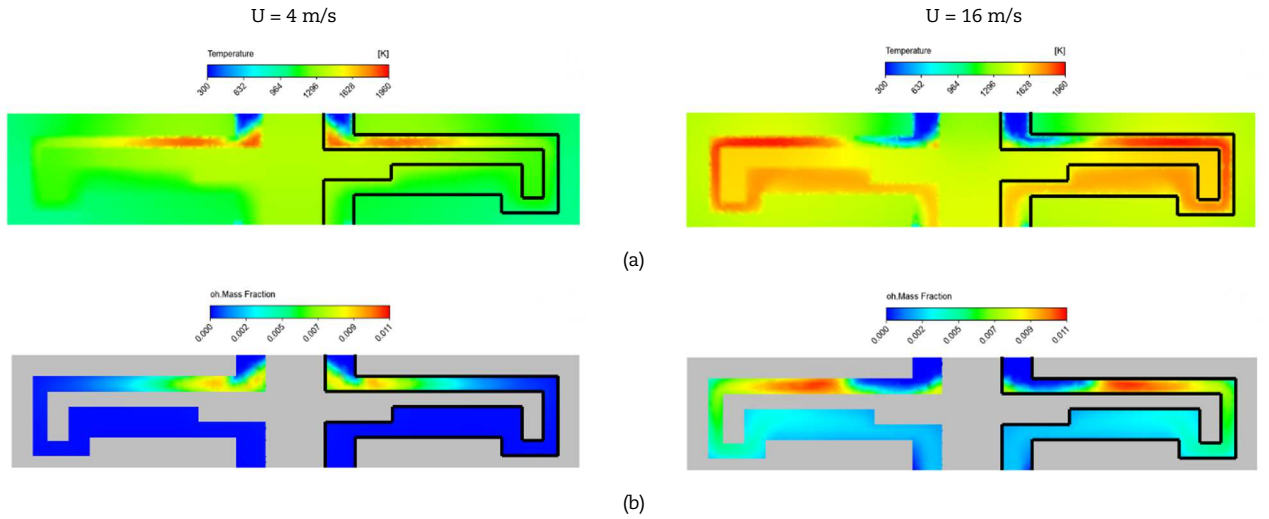


Fig. 4. Contour of (a) temperature and, (b) OH mass fraction for U = 4, 16 m/s, φ = 1 and λ_s = 6.7 W/m.K.

3. Results and Discussion

The present micro-combustor is designed for thermophotovoltaic (TPV) applications, in which a uniform wall temperature distribution is essential for enhancing system performance. The present section investigates the effects of inlet velocity, equivalence ratio, and wall thermal conductivity on temperature distribution and OH mass fraction along the flow centerline. Four inlet velocities (4, 8, 12, and 16 m/s) are analyzed. Equivalence ratios of 0.5, 0.8, 1.0, and 1.2 are considered to assess mixture effects, while wall thermal conductivity is evaluated using quartz, titanium, and steel with values of 1.4, 6.7, and 12.63 W/m·K, respectively. The resulting effects on peak and average temperatures, temperature uniformity, deviation from mean values, and flame position are analyzed. In addition, system thermal efficiency and power output are quantified.

3.1. Effect of inlet velocity on combustion characteristics

The present section examines the effect of inlet flow velocity on combustion characteristics, with particular emphasis on temperature distribution and OH mass fraction along the flow centerline. Four inlet velocities (4, 8, 12, and 16 m/s) are analyzed. The resulting influence on flame position, peak and mean temperatures, temperature uniformity, and deviation from the average temperature is evaluated. The inlet velocity was investigated over the range of 4–16 m/s to characterize its effects on flame position, temperature distribution, OH radical formation, and thermal efficiency within the stable operating regime of the present micro-combustor. This velocity range is within the order of magnitude commonly considered in previous studies of hydrogen-fueled micro-combustors and related microscale combustion systems [45–52]. It should be noted that the upper value of 16 m/s represents the maximum inlet velocity investigated in the present study and does not necessarily correspond to the ultimate blow-off limit of the combustor. At higher velocities, substantially larger reactant mass-flow rates and greater demands on flow-supply and control equipment may arise in microscale systems. Therefore, characterization of the flame response at significantly higher velocities, including flame lift-off and blow-off limits, is beyond the scope of the present study and is identified as an important direction for future investigation.

Figure 4 shows temperature and OH mass fraction distributions in the combustor mid-plane for U = 4 and 16 m/s, at φ = 1 and λ_s = 6.7 W/m·K. Increasing inlet velocity results in a downstream shift of the maximum temperature location, as illustrated in Fig. 4(a). This shift is caused by the reduced residence time at higher velocities, which limits preheating and reduces the enthalpy accumulation of the incoming mixture. Consequently, flame stabilization occurs further downstream. A comparable trend is observed for OH in Fig. 4(b), where the peak OH concentration also migrates downstream. This behavior is consistent with the dependence of radical formation on temperature, as the highest OH production occurs in the high-temperature reaction zone. Therefore, the OH peak follows the flame displacement, indicating a downstream shift in the main reaction region. Overall, inlet velocity strongly affects both thermal and chemical fields.

Figure 5 shows the centerline distributions of temperature and OH mass fraction for inlet velocities of 4–16 m/s. As illustrated in Fig. 5(a), the maximum temperature increases progressively with inlet velocity, reaching 1808 K, 1882 K, 1898 K, and 1933 K at centerline positions 55, 84, 125, and 130, respectively. This behavior indicates that increasing inlet velocity enhances the overall heat release rate in the reaction zone due to the higher fuel mass flow rate, which increases the available chemical energy. The observed downstream displacement of the peak temperature is primarily caused by the reduced residence time of the reacting mixture, which delays preheating and shifts the flame location downstream.

Figure 5(b) shows the corresponding OH mass fraction along the flow centerline. With increasing inlet velocity, the location of the maximum OH concentration similarly shifts downstream, occurring at positions 41, 65, 79, and 93 for velocities of 4, 8, 12, and 16 m/s, respectively. The maximum OH mass fractions are 0.0093, 0.0103, 0.0106, and 0.0109, demonstrating a clear increase with higher velocities. This behavior is directly related to the higher fuel concentration entering the reaction zone, which accelerates the rates of the initial, chain, and branching reactions. As a result, more active radicals, particularly OH, are produced in the reaction region. The downstream displacement of the peak OH concentration corresponds to the shift of the high-temperature zone, illustrating the strong coupling between thermal and chemical dynamics in the combustor.

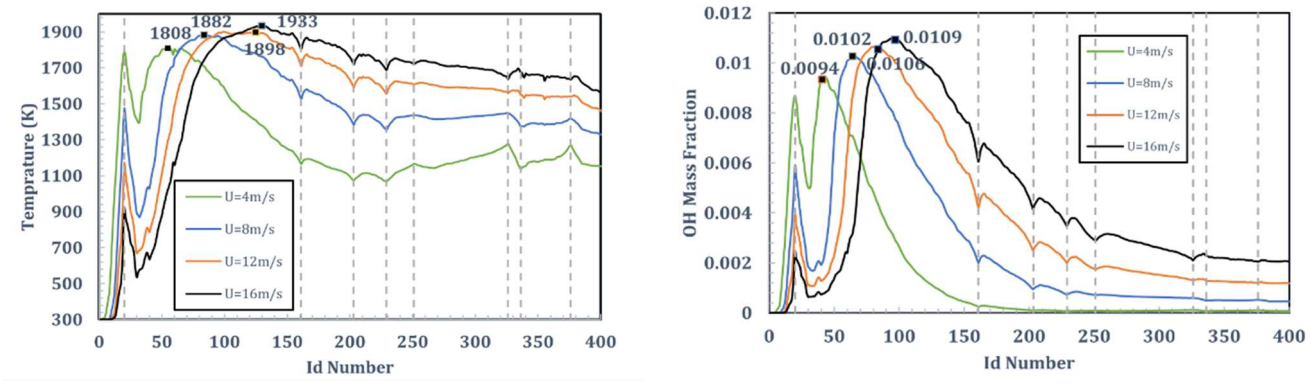
Furthermore, these trends reveal a complex interplay between inlet velocity, residence time, and radical formation. While higher velocities increase the overall fuel throughput and promote higher peak temperatures and radical production, they also reduce the preheating of the incoming mixture, which shifts the flame location downstream. This indicates that optimizing the inlet velocity is critical for controlling both flame stability and radical distribution, which are essential parameters for applications such as thermophotovoltaic systems. The results highlight that careful balancing of flow rate and preheating is necessary to maximize combustion efficiency while ensuring proper flame anchoring and uniformity of reactive species within the micro-combustor.

Figure 6(a) presents the variation of flame front position with inlet flow velocity. The flame front is defined as the point along the flow centerline at which 50% of the incoming fuel is consumed. This location is determined by identifying the 50% fuel-consumption isoline and extracting its intersection with the centerline. As the inlet velocity increases from 4 to 16 m/s, the flame front moves downstream from positions 13, 17, and 20 to 62, respectively, demonstrating a pronounced velocity-dependent displacement.

At lower inlet velocities, the residence time of the mixture in the reaction zone is relatively long, allowing sufficient time for heat transfer and chemical reactions to initiate near the chamber inlet. As a result, the flame forms closer to the inlet, and the reaction zone is concentrated near the upstream region. In contrast, higher inlet velocities reduce the residence time, which delays the attainment of the critical thermal and chemical conditions required for chain reactions. Consequently, the mixture travels a longer distance before reaching autoignition conditions, shifting the flame front downstream. This downstream displacement is also influenced by enhanced mass transfer at higher velocities. Increased flow rates accelerate the transport of both fuel and oxidizer into the reaction zone, but they simultaneously reduce the preheating effect of the incoming fluid. The combination of reduced thermal residence time and faster convective transport leads to a flame that is both elongated and displaced further from the inlet. Moreover, the shift in flame front location has direct consequences for the spatial distribution of temperature and reactive species within the chamber. As the flame moves downstream, the region of peak temperature and maximum radical concentrations, including OH, is also displaced, consistent with the trends observed in Figs. 4 and 5.

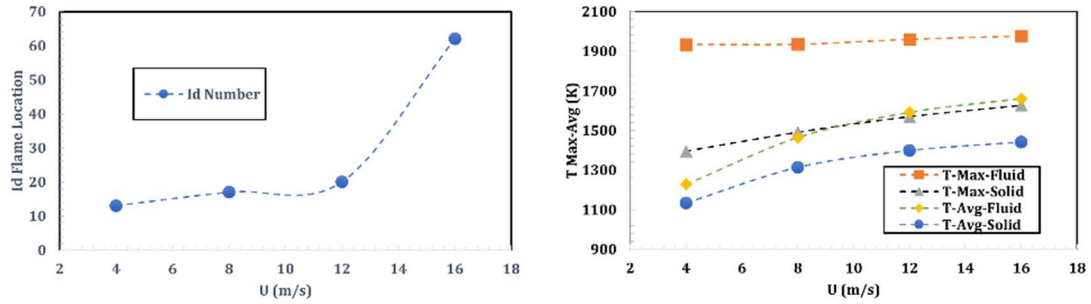
The displacement of the flame front alters the structure and thickness of the reaction zone, which may significantly affect flame stability, heat release characteristics, and temperature uniformity along the walls. These factors play a crucial role in determining micro-combustor performance, especially for thermophotovoltaic system applications.

Figure 6(b) presents the variations of maximum and average temperatures in the fluid and solid domains with increasing inlet velocity. As the inlet velocity increases from 4 to 16 m/s, the maximum fluid temperature increases progressively from 1933 K, 1934 K, and 1959 K to 1976 K, whereas the average fluid temperature rises from 1227 K to 1660 K. In the solid, the maximum temperature increases from 1394 K to 1626 K, and the average solid temperature rises from 1133 K to 1440 K, showing a clear upward trend in both phases. This indicates that higher inlet velocities not only elevate peak temperatures but also increase the overall thermal energy contained within the system. The observed behavior results from a combination of two main mechanisms. First, higher inlet velocities increase the mass flow rate of reactants entering the combustion zone, enhancing the rate of chemical reactions and leading to higher energy release per unit time. This contributes to the observed rise in maximum temperatures. Second, increased flow velocity strengthens convective heat transfer within the fluid and conductive heat transfer to the solid walls, facilitating more rapid and efficient distribution of thermal energy. As a result, the average temperature in both the fluid and solid increases, and the temperature gradients across the chamber become less steep, improving thermal uniformity. These trends are closely linked to other combustion characteristics observed in the study. As discussed in Figs. 4 to 6(a), higher inlet velocities shift the flame front downstream and displace the region of peak OH radical concentration. This downstream shift affects the local heating of the walls, altering the location and intensity of heat fluxes from the flame to the chamber surfaces. Despite the flame moving downstream, the combined effect of increased reaction rates and enhanced convective and conductive heat transfer results in higher maximum and average temperatures throughout the chamber, demonstrating that inlet velocity strongly controls both the thermal and chemical behavior of the micro-combustor.



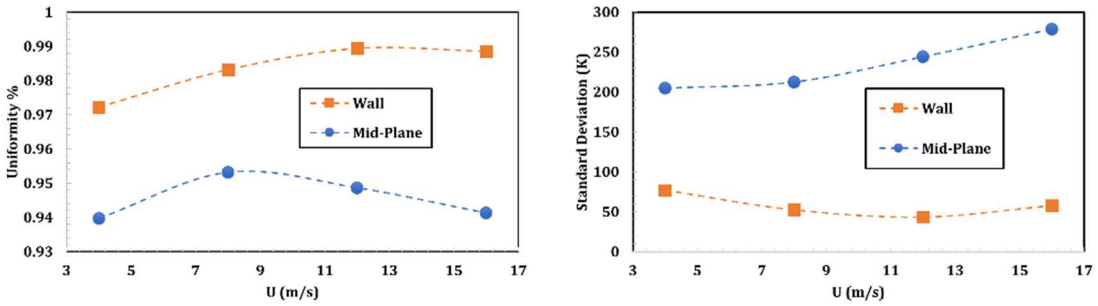
(a) (b)

Fig. 5. Variations of (a) temperature and, (b) OH mass fraction along the flow centerline for different velocities, $\varphi = 1$, and $\lambda_s = 6.7$ W/m.K.



(a) (b)

Fig. 6. Effect of different inlet velocity on (a) flame location, (b) maximum and average temperatures in the solid and fluid, $\varphi = 1$ and $\lambda_s = 6.7$ W/m.K.



(a) (b)

Fig. 7. Effect of different inlet velocity on (a) temperature uniformity, (b) standard deviation of temperature, $\varphi = 1$ and $\lambda_s = 6.7$ W/m.K.

Figure 7 investigates the effect of inlet velocity on temperature uniformity and deviation from the mean temperature in both the mid-plane of the combustion chamber and the chamber walls, at an equivalence ratio of 1 and a thermal conductivity of 6.7 W/m·K. The deviation from the mean temperature is defined as the difference between the temperature at each computational cell and the overall average temperature of the domain; smaller deviations correspond to higher temperature uniformity. Temperature uniformity is a critical parameter, as it ensures consistent heat generation and maximizes energy conversion efficiency, particularly in applications such as thermophotovoltaic systems. Figure 7(a) presents the influence of inlet velocities (4–16 m/s) on temperature uniformity in both the mid-plane and wall regions. The results indicate that the mid-plane temperature uniformity reaches its maximum at 8 m/s, while the highest uniformity along the wall is obtained at 12 m/s. The increase in uniformity with velocity up to these optimal points is primarily due to enhanced convective heat transfer, which promotes more even distribution of thermal energy and reduces localized hot or cold spots. Beyond these velocities, temperature uniformity decreases: in the mid-plane, the reduced residence time limits complete fuel–air combustion, while along the wall, enhanced heat losses and the development of complex flow structures, such as recirculation zones and non-uniform velocity profiles, disrupt uniform heat transfer.

Figure 7(b) further illustrates these trends by plotting the deviation from the mean temperature. In the mid-plane, the deviation continuously increases with inlet velocity, indicating that higher velocities amplify temperature differences between points and reduce overall uniformity. This occurs because, while higher velocities accelerate reaction rates and convective heat transfer, they simultaneously reduce residence time and increase heat losses, preventing full thermal equilibration. In contrast, along the chamber wall, the deviation decreases as velocity increases from 4 m/s to 12 m/s, reflecting improved uniformity due to more effective convective and conductive heat transfer from the fluid. Beyond 12 m/s, the deviation increases again due to higher wall heat losses and the influence of complex flow patterns, confirming that excessive velocity can reduce wall temperature uniformity. These results highlight the complex, region-dependent influence of inlet velocity on temperature uniformity. Optimizing inlet velocity is therefore essential to balance convective heat transfer, chemical reaction rates, residence time, and heat loss. Achieving this balance ensures uniform temperatures in both the fluid and solid phases, improving flame stability, reaction efficiency, and the overall performance of micro-combustor systems.

3.2. Effect of equivalence ratio on combustion characteristics

This section examines the influence of equivalence ratio on combustion behavior, focusing on temperature distribution and OH mass fraction in the reaction zone. Equivalence ratios of 0.5, 0.8, 1.0, and 1.2 are considered at a constant inlet velocity of 8 m/s and thermal conductivity of 6.7 W/m·K. The rich condition of $\varphi = 1.2$ enables examination of the transition from stoichiometric to fuel-rich combustion and allows the effects of oxygen limitation on flame structure, radical formation, temperature distribution, and thermal efficiency to be identified.

The results are analyzed along the flow centerline of the combustor cross-section. The effects of equivalence ratio on flame front position, maximum and average temperatures in the fluid and solid domains, temperature uniformity, and deviation from the mean temperature are assessed.

Figure 8(a) presents mid-plane temperature contours for $\varphi = 0.5$ and 1.2 at U = 8 m/s and $\lambda_s = 6.7$ W/m·K. The results demonstrate that higher equivalence ratios result in increased maximum temperatures and a downstream displacement of the high-temperature zone along the flow path. At lower equivalence ratios (lean mixtures), the reduced fuel content limits the rate of chemical reactions and the total energy release, resulting in lower maximum temperatures and a flame that is closer to the inlet. For equivalence ratios above 1 (rich mixtures), the flame continues to shift downstream due to the higher thermal energy generated, but the excess fuel can also create localized regions of incomplete combustion, modify the temperature distribution and broaden the reaction zone.

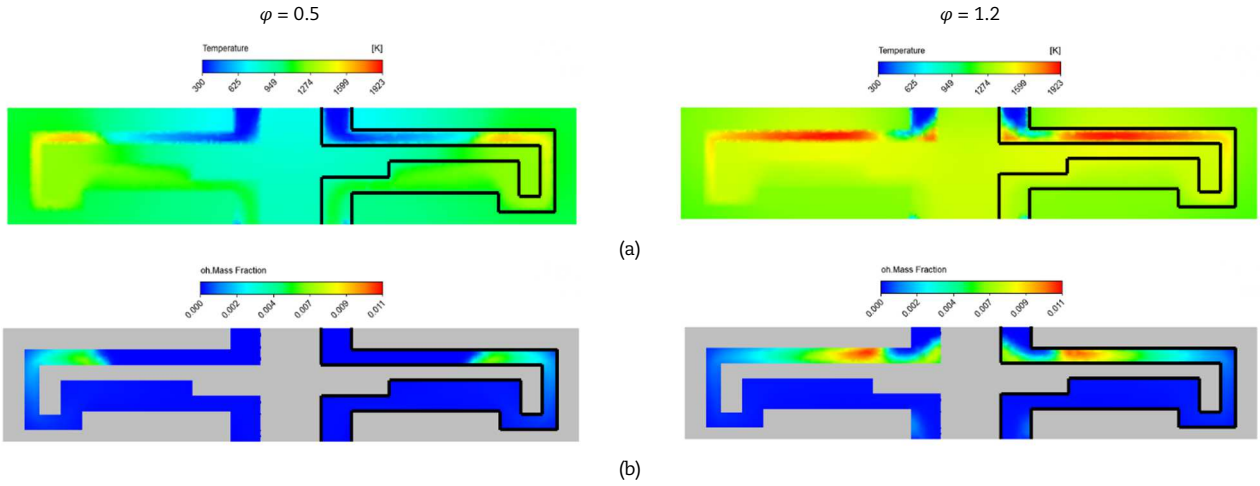


Fig. 8. Contour of (a) temperature and, (b) OH mass fraction for φ = 0.5, 1.2, U = 8 m/s and λ_s = 6.7W/m.K.

Figure 8(b) illustrates the contours of OH mass fraction for equivalence ratios of 0.5 and 1.2 under the same flow and thermal conditions. The results indicate that as the equivalence ratio increases from 0.5 to 1.2, the location of the maximum OH concentration moves downstream, corresponding to the displacement of the flame front observed in the temperature distribution. This shift occurs because higher equivalence ratios increase the rate of chain and branching reactions, generating more active radicals such as OH further along the flow. When the equivalence ratio exceeds one, the peak OH mass fraction moves slightly upstream toward the inlet. This upstream shift is associated with fuel-rich conditions, in which increased fuel concentration near the inlet intensifies local reaction activity prior to downstream development, and the abundance of unreacted fuel facilitates earlier radical generation. The trends in Figs. 8(a) and 8(b) demonstrate the strong coupling between equivalence ratio, flame structure, temperature distribution, and radical generation. Increasing the equivalence ratio not only elevates the maximum temperature but also displaces the reaction zone and alters the spatial distribution of OH radicals.

Figure 9 shows temperature distributions along the flow centerline for equivalence ratios of 0.5, 0.8, 1.0, and 1.2. As illustrated in Fig. 9(a), the maximum temperature increases progressively with equivalence ratio, attaining 1618 K, 1777 K, 1882 K, and 1897 K at centerline locations 131, 84, 84, and 84, respectively. This behavior demonstrates a direct dependence of thermal energy release in the reaction zone on fuel concentration. At low equivalence ratios (lean conditions), the presence of excess oxidizer limits the efficiency of combustion. Not all the chemical potential of the fuel–air mixture is released, and the excess oxidizer absorbs part of the released energy, resulting in lower flame temperatures and a delayed heat release along the flow direction. Consequently, the peak temperature occurs further downstream in the chamber under lean conditions, as indicated by point 131 along the centerline for an equivalence ratio of 0.5.

As the equivalence ratio approaches stoichiometric conditions (φ = 1), the combustion reaction becomes more complete, allowing the chemical energy of the fuel to be converted into thermal energy more efficiently. This results in a significant increase in maximum temperature, observed at 1882 K along point 84 on the centerline. In this regime, the formation of stable products such as H_2O and OH radicals are maximized, releasing higher reaction enthalpy and intensifying heat transfer to the surrounding fluid. The reaction zone becomes more concentrated, and the flame front shifts upstream relative to lean mixtures due to higher local reaction rates and energy release.

For equivalence ratios above 1 (rich mixtures), the maximum temperature increases slightly to 1897 K, occurring at the same centerline position as the stoichiometric case. In rich conditions, although there is excess fuel, the reaction rate near the inlet remains high due to the abundant fuel availability, while incomplete combustion begins to occur in some regions, leading to localized heat release. In confined geometries such as micro-channels or small combustion chambers, these effects concentrate energy in a limited volume, maintaining a high maximum temperature along the flow centerline. Overall, the results demonstrate that increasing equivalence ratio enhances both the magnitude and upstream location of maximum temperature due to higher reaction rates and more effective energy conversion, highlighting the strong dependence of flame thermal characteristics on the fuel–air mixture composition.

Figure 9(b) illustrates the effect of equivalence ratios of 0.5, 0.8, 1, and 1.2 on the OH mass fraction along the flow centerline in the mid-plane of the combustion chamber, at an inlet velocity of 8 m/s and a wall thermal conductivity of 6.7 W/m·K. The maximum OH mass fractions for equivalence ratios of 0.5, 0.8, 1, and 1.2 are 0.0059, 0.0087, 0.0102, and 0.0095, occurring at points 125, 65, 65, and 60 along the centerline, respectively.

In lean mixtures (φ = 0.5), the fuel content is low, which limits reaction rates and overall reactivity. As a result, the flame temperature is relatively low, and the production of active radicals such as OH is restricted, leading to a lower peak OH concentration. Gradually increasing the equivalence ratio toward stoichiometric conditions enhances the fuel-to-oxidizer ratio, increasing the reaction rates and raising the flame temperature. This promotes more complete chemical reactions, generating higher concentrations of OH radicals. At stoichiometric conditions (φ = 1), the reactions reach their optimal efficiency, resulting in the maximum observed OH mass fraction of 0.0102, and the peak location shifts upstream to point 65 along the centerline, reflecting the stronger and more concentrated reaction zone. For equivalence ratios above 1 (rich mixtures), although the fuel content is higher, the limited availability of oxygen prevents complete oxidation. In this regime, incomplete products such as H_2 are formed, and the reaction enthalpy is partially reduced, leading to a slight decrease in flame temperature. Consequently, the production of OH radicals decrease, with the maximum OH mass fraction dropping to 0.0095 and the peak location moving slightly closer to the inlet (point 60). This trend demonstrates the delicate balance between fuel availability and oxidizer concentration: while increasing fuel initially enhances radical generation, excess fuel in oxygen-limited conditions reduces the formation of active species, altering the spatial distribution and intensity of the reaction zone.

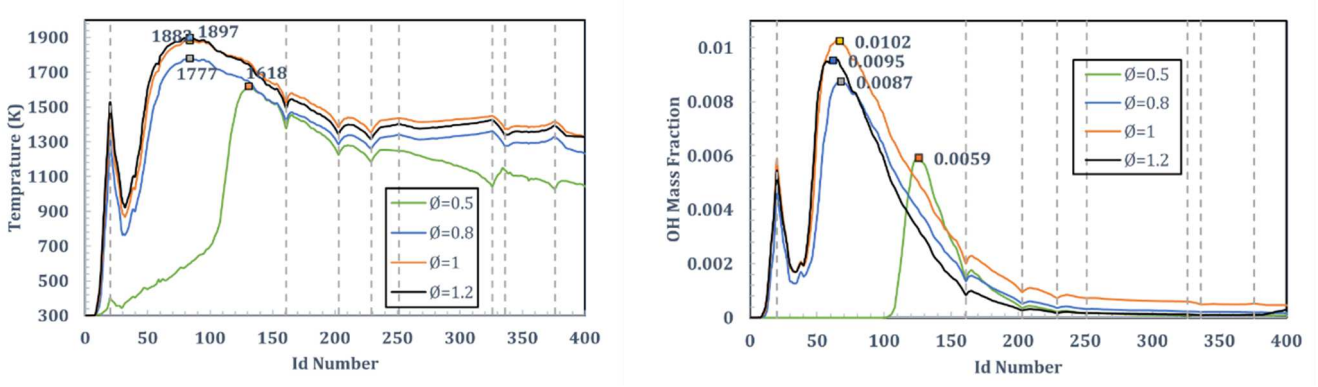


Fig. 9. Variations of (a) temperature and, (b) OH mass fraction along the flow centerline for different equivalence ratios, U = 8 m/s and λ_s = 6.7 W/m.K.

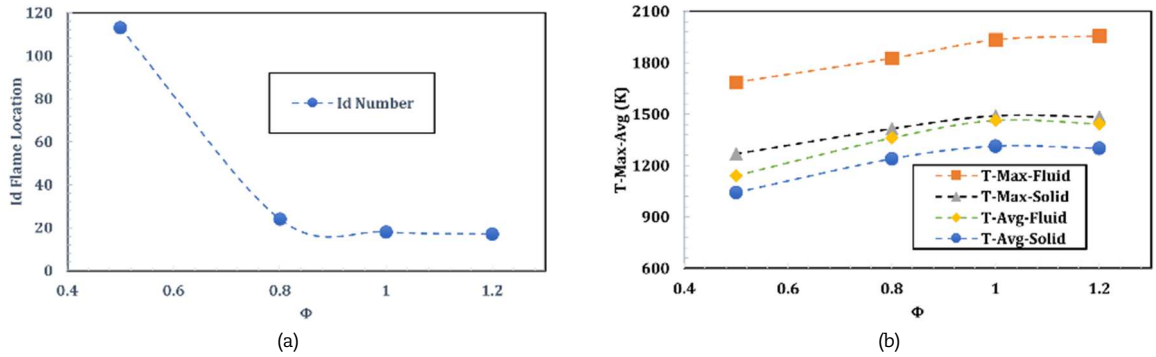


Fig. 10. Effect of different equivalence ratio on (a) flame location, (b) maximum and average temperature of the fluid and solid domain, U = 8 m/s and λ_s = 6.7 W/m.K.

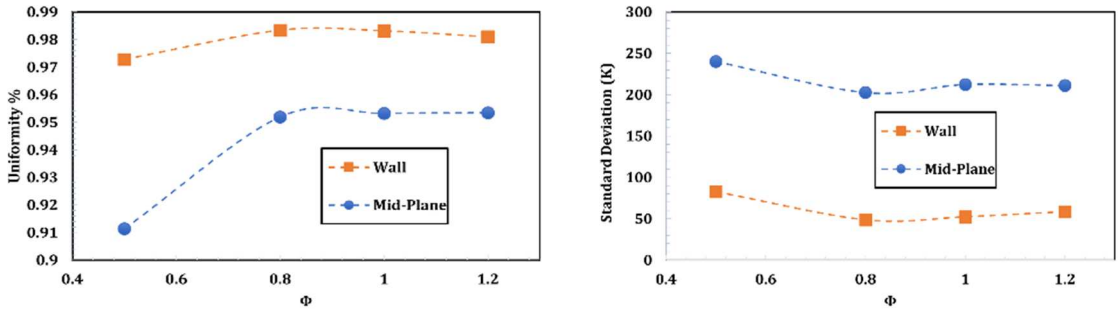
Figure 10 illustrates the effect of different equivalence ratios on flame location along the flow centerline in the mid-plane, as well as the maximum and average temperatures of the fluid and solid, at an inlet velocity of 8 m/s and a wall thermal conductivity of 6.7 W/m·K. According to Fig. 10(a), increasing the equivalence ratio causes the flame location to shift significantly toward the inlet, occurring at points 113, 24, 18, and 17 along the flow centerline for equivalence ratios of 0.5, 0.8, 1, and 1.2, respectively. The flame corresponding to the lean condition (φ= 0.5) is located farthest downstream, indicating a longer ignition delay. This behavior arises from the lower fuel concentration and weaker reaction intensity in lean mixtures, which require a longer distance for the mixture to reach the necessary thermal and chemical conditions for ignition. As the equivalence ratio increases, the mixture reactivity improves due to higher fuel availability, leading to faster heat release and earlier initiation of combustion, thereby shifting the flame toward the inlet.

Figure 10(b) presents the variations of maximum and average temperatures in both the fluid and solid phases with changing equivalence ratio. The maximum fluid temperatures for equivalence ratios of 0.5, 0.8, 1, and 1.2 are 1686 K, 1826 K, 1934 K, and 1956 K, respectively, while the corresponding maximum solid temperatures are 1268 K, 1415 K, 1490 K, and 1484 K. A clear increasing trend in both maximum and average temperatures is observed as the equivalence ratio increases from lean conditions up to the stoichiometric point. This increase is primarily attributed to more efficient combustion, as the fuel–oxidizer mixture approaches the optimal proportion for complete chemical reaction, resulting in higher heat release rates and enhanced energy conversion into thermal energy. Consequently, both the fluid and solid phases experience higher temperatures due to stronger heat generation and more effective heat transfer from the reacting flow to the solid walls.

However, beyond the stoichiometric condition (φ = 1), the thermal behavior begins to change. Although the maximum fluid temperature continues to increase slightly at an equivalence ratio of 1.2, the maximum solid temperature shows a slight decrease, and the overall trend of average temperatures indicates a reduction in thermal efficiency. This is due to oxygen limitation in rich mixtures, which prevents complete oxidation of the fuel and leads to the formation of intermediate species such as CO and H_2 instead of fully oxidized products like CO_2 and H_2O. As a result, a portion of the chemical energy remains unconverted, reducing the effective heat release. Additionally, incomplete combustion weakens heat transfer to the solid walls, leading to a slight drop in solid temperature despite the locally high fluid temperature.

Figure 11 illustrates the influence of equivalence ratio on temperature uniformity and deviation from the mean temperature in both the mid-plane and wall regions, under conditions of U = 8 m/s and λ_s = 6.7 W/m·K. The results in Fig. 11(a) indicate that temperature uniformity is strongly affected by increasing equivalence ratio across the combustor. In both the mid-plane and the external wall, temperature uniformity improves as the equivalence ratio increases up to approximately 0.8. This enhancement is associated with a more balanced fuel–air mixture, which promotes more complete combustion, higher and more evenly distributed heat release, and a reduction in localized cold regions caused by excess oxidizer in lean conditions. As a result, temperature gradients decrease and the thermal field becomes more homogeneous.

As the equivalence ratio increases beyond 0.8, the temperature uniformity index begins to decline in both regions. This deterioration is primarily due to the onset of oxygen limitation in richer mixtures, which restricts complete combustion and leads to spatially non-uniform heat release. In such conditions, some regions of the flow experience intense reactions while others remain relatively under-reacted, creating localized hot and cold spots. Additionally, variations in reaction rates and species concentrations contribute to uneven energy distribution, further reducing overall thermal uniformity.



(a) (b)

Fig. 11. Effect of different equivalence ratio on (a) temperature uniformity, (b) standard deviation of temperature, U = 8 m/s and λ_s = 6.7 W/m.K.

Figure 11(b) presents the corresponding variations in deviation from the mean temperature, providing a complementary perspective on thermal uniformity. The results show that, as the equivalence ratio increases up to approximately 0.8, the deviation from the mean temperature decreases in both the mid-plane and wall regions. This trend confirms that the temperature field becomes more uniform under these conditions, as the heat generated by combustion is more effectively distributed across the geometry. The reduction in deviation is consistent with enhanced reaction completeness and more uniform energy release. For equivalence ratios greater than 0.8, the deviation from the mean temperature increases in both regions, indicating a decline in temperature uniformity. This behavior is again attributed to incomplete combustion under fuel-rich conditions, where insufficient oxygen leads to uneven reaction progress and non-uniform heat generation. Furthermore, the formation of intermediate species and the reduction in effective heat release intensify spatial temperature variations. Consequently, the thermal field becomes less homogeneous, which may negatively impact system performance, particularly in applications requiring uniform heat distribution such as thermophotovoltaic systems.

3.3. Effect of thermal conductivity variations on combustion characteristics

This section examines the influence of thermal conductivity on combustion behavior, focusing on temperature distribution and OH radical mass fraction within the reaction zone. Thermal conductivity strongly affects heat exchange between the solid and fluid domains, thereby impacting flame stability, heat recirculation processes, and overall combustion efficiency.

In the present study, quartz, titanium, and steel were selected as representative wall materials with different thermal conductivity levels of 1.4, 6.7, and 12.63 W/m·K, respectively. As indicated by Eq. (6), heat conduction through the solid wall is governed by the thermal conductivity. Therefore, these materials were considered to represent a range of wall thermal conductivity levels and to evaluate their influence on heat transfer between the combustion gases and the solid wall. The simulations were conducted at an equivalence ratio of 0.5 and an inlet flow velocity of 8 m/s. Accordingly, the present comparison primarily focuses on the effect of different wall thermal conductivity levels on the combustion and heat-transfer characteristics, rather than providing a comprehensive assessment of the individual thermophysical effects of quartz, titanium, and steel.

The results are presented along the line defined as the flow centerline in the mid-plane of the geometry shown in Fig. 1. In addition, the effects of thermal conductivity variations on flame location, maximum and average temperatures, temperature uniformity, and deviation from the mean temperature are examined to provide a detailed understanding of the influence of solid-phase thermal properties on combustion behavior within the chamber.

Figure 12(a) shows mid-plane temperature distributions for different wall thermal conductivities (1.4, 6.7, and 12.63 W/m·K) at U = 8 m/s and φ = 0.5. It is observed that higher wall thermal conductivity results in an upstream shift of the flame front toward the inlet. This behavior is primarily attributed to enhanced heat transfer between the reaction zone and the solid wall. With higher thermal conductivity, the heat transfer time scale within the wall decreases, allowing thermal energy generated in the flame region to be conducted more rapidly upstream through the solid. This process effectively increases the temperature of the incoming fuel–air mixture, facilitating the onset of chain-branching reactions closer to the inlet. As a result, the preheating effect becomes stronger, and the flame stabilizes in a more upstream position.

However, increasing the wall thermal conductivity also intensifies heat losses from the reaction zone. At higher conductivity values, a larger portion of the generated thermal energy is conducted away from the flame, reducing the local peak temperature within the combustion region. This reduction in maximum temperature can weaken the overall reaction intensity and, under extreme conditions, may lead to partial flame quenching. Therefore, while enhanced thermal conductivity improves upstream heat recirculation and flame stabilization, it simultaneously introduces a competing effect through increased heat dissipation.

Figure 12(b) presents the contours of OH mass fraction for the same conditions. Consistent with the temperature field, the distribution of OH radical shifts toward the inlet as the wall thermal conductivity increases. This shift reflects the upstream movement of the reaction zone, where the highest rates of chemical reactions and radical formation occur. The increased preheating of the incoming mixture enhances the rates of initial decomposition and chain-branching reactions, leading to higher production of active radicals such as OH. Consequently, as the wall thermal conductivity increases up to an optimal level, the maximum OH concentration within the chamber also increases. At the highest thermal conductivity considered (12.63 W/m·K), the maximum of OH mass fraction reaches its peak value, indicating intensified chemical activity in the upstream region. Nevertheless, the accompanying increase in heat loss reduces the local flame temperature, which may limit further growth in radical concentration if conductivity is increased beyond this range. So, thermal conductivity plays a dual role in combustion behavior: it enhances preheating and reaction initiation while simultaneously increasing heat losses, thereby influencing both flame structure and chemical activity within the chamber.

Figure 13 shows temperature distributions on the mid-plane and flow centerline for wall thermal conductivities of 1.4, 6.7, and 12.63 W/m·K at U = 8 m/s and φ = 0.5. The results in Fig. 13(a) demonstrate that the maximum temperature increases with thermal conductivity, attaining 1591 K, 1618 K, and 1628 K, respectively.

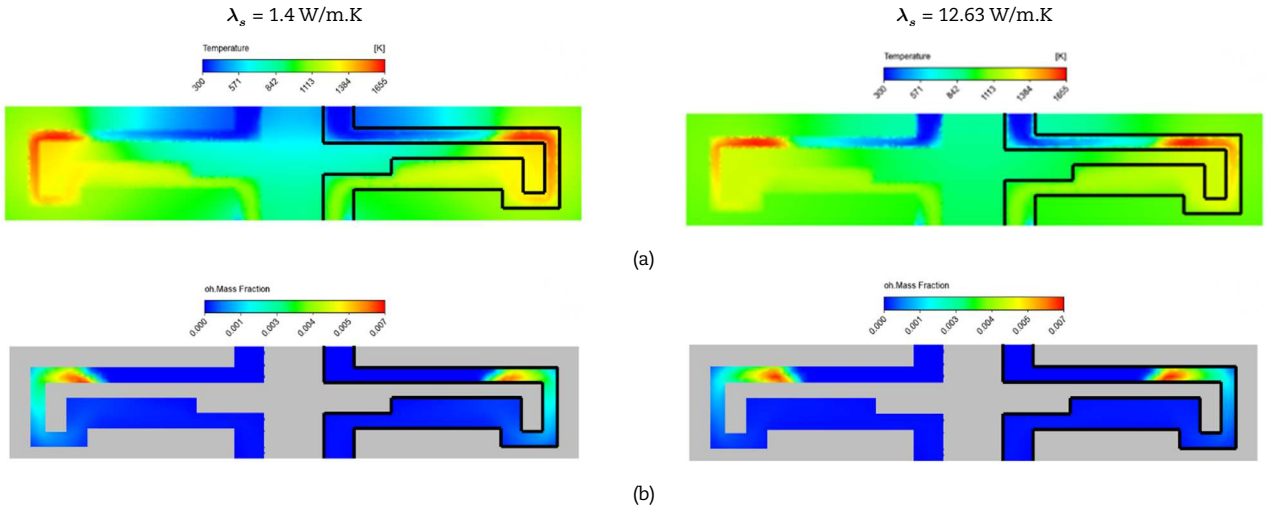


Fig. 12. Contour of (a) temperature and, (b) OH mass fraction for λ_s = 1.4 and 12.63 W/m.K, U = 8 m/s and φ = 0.5.

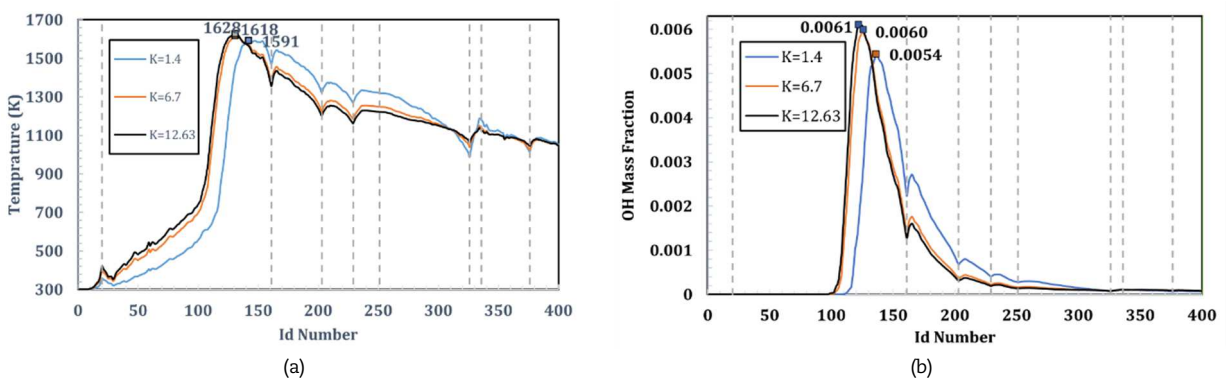


Fig. 13. Variations of (a) temperature and, (b) OH mass fraction along the flow centerline for different thermal conductivity coefficient velocities, φ = 0.5, and U = 8 m/s.

The corresponding peak locations at centerline positions 142, 131, and 131 reveal both an increase in temperature magnitude and an upstream displacement of the reaction zone as thermal conductivity increases. This behavior is primarily attributed to enhanced heat recirculation through the solid walls at higher thermal conductivity. As the wall conductivity increases, heat generated in the reaction zone is conducted more efficiently upstream, raising the temperature of the incoming fuel–air mixture.

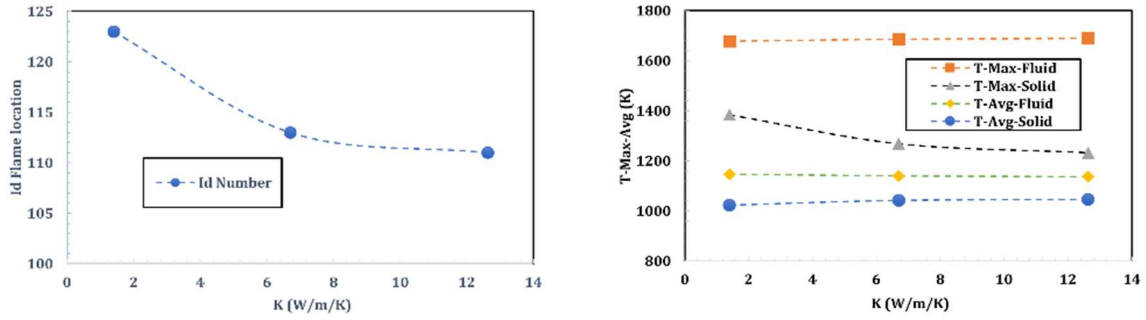
Figure 13(b) presents the corresponding variations in OH mass fraction along the mid-plane and flow centerline. The maximum OH mass fraction increases from 0.0054 to 0.0059 and 0.0061 as the thermal conductivity rises from 1.4 to 6.7 and 12.63 W/m·K, respectively. The locations of these peak values also shift upstream, occurring at positions 136, 125, and 123 along the centerline. This trend closely follows the temperature distribution, reflecting the strong dependence of OH radical formation on local temperature and reaction intensity.

With increasing thermal conductivity, the elevated temperature levels enhance the rates of elementary reactions responsible for OH production, particularly chain-branching reactions involving H, O, and intermediate species. The accelerated reaction kinetics lead to a higher concentration of active radicals within the flame region. Additionally, improved heat conduction contributes to a more distributed thermal field within the reaction zone, which can extend the region over which favorable conditions for OH formation exist.

Figure 14 presents the effect of wall thermal conductivity on flame position along the mid-plane and flow centerline, together with its impact on the maximum and average temperatures of the fluid and solid domains, under conditions of U = 8 m/s and φ = 0.5. According to Fig. 14(a), increasing the thermal conductivity shifts the flame location upstream to positions 123, 113, and 111 along the flow centerline, respectively. This trend clearly indicates that higher thermal conductivity promotes earlier flame stabilization closer to the inlet. The underlying mechanism is associated with enhanced heat transfer from the high-temperature reaction zone to the colder incoming mixture. As thermal conductivity increases, heat is conducted more efficiently through the solid wall, elevating the temperature of the incoming flow. This preheating effect facilitates earlier initiation of chemical reactions, allowing the flame to anchor closer to the inlet region.

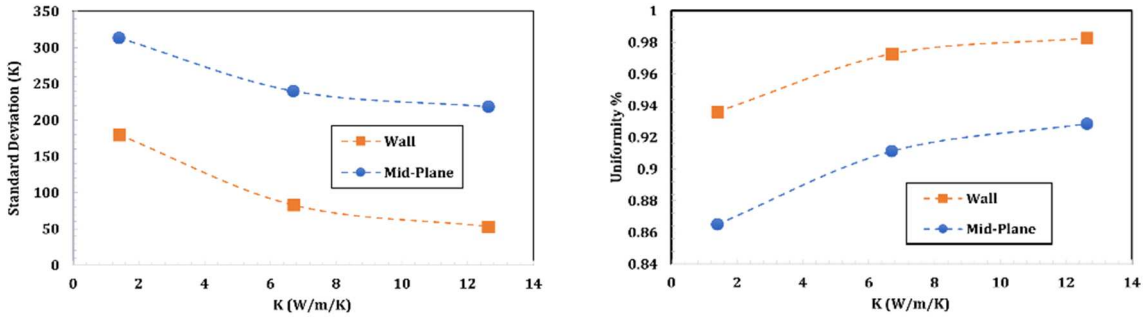
Figure 14(b) presents the variations in maximum and average temperatures of both the fluid and solid phases with changing thermal conductivity. The results show that increasing the thermal conductivity from 1.4 to 6.7 and 12.63 W/m·K does not significantly affect the maximum or average fluid temperature, nor the average solid temperature. This behavior suggests that the overall energy balance within the system remains relatively unchanged, and the combustion process continues to release a similar amount of heat regardless of wall conductivity. In other words, the global thermal field is governed primarily by the combustion chemistry and flow conditions rather than by variations in wall thermal properties within the studied range.

However, a noticeable effect is observed in the maximum solid temperature, which decreases from 1384 K to 1268 K and 1232 K as thermal conductivity increases. This reduction can be explained by the enhanced ability of the solid material to redistribute thermal energy. At lower thermal conductivity, heat tends to accumulate in localized regions, leading to higher peak temperatures. In contrast, higher conductivity promotes more uniform heat spreading within the solid, reducing thermal gradients and dissipating energy away from hot spots more effectively. As a result, peak temperatures in the solid phase are diminished, even though the average temperature remains relatively constant.



(a) (b)

Fig. 14. Effect of different thermal conductivity on (a) flame location, (b) maximum and average temperatures of fluid and solid domain, U = 8 m/s and an φ = 0.5.



(a) (b)

Fig. 15. Effect of different thermal conductivity changes on (a) temperature uniformity, (b) deviation from the average temperature, in the geometry and wall cross-section plane with U = 8 m/s and an φ = 0.5.

Figure 15 presents the influence of thermal conductivity variations (1.4, 6.7, and 12.63 W/m·K) on temperature uniformity and deviation from the mean temperature along the mid-plane and wall surfaces of the geometry under conditions of U = 8 m/s and φ = 0.5. As shown in Fig. 15(a), increasing thermal conductivity leads to a noticeable improvement in temperature uniformity across different regions of the combustion chamber, particularly in the mid-plane and along the outer wall. This behavior is primarily attributed to the enhanced ability of materials with higher thermal conductivity to redistribute thermal energy more efficiently. As heat generated in the reaction zone is conducted more rapidly through the solid structure, temperature gradients are reduced, resulting in a more homogeneous thermal field. Consequently, the temperature uniformity index increases, indicating a more even distribution of heat within the geometry.

Figure 15(b) further confirms this trend by showing that increasing thermal conductivity reduces the deviation from the mean temperature in both the mid-plane and outer wall regions. Since the deviation from the mean temperature quantifies the extent of temperature fluctuations within the domain, its reduction directly indicates improved temperature uniformity. The enhanced heat conduction enables faster thermal equilibration throughout the geometry, minimizing local temperature extremes and bringing individual cell temperatures closer to the overall average.

3.4. Investigation of thermal efficiency and total power

Overall thermal efficiency is one of the primary indicators used to evaluate combustion system performance, representing the fraction of the fuel's chemical energy that is converted into useful energy during the combustion process. Figure 16 illustrates the effect of inlet flow velocity on overall thermal efficiency, radiative thermal efficiency, thermophotovoltaic (TPV) system power, and total thermal power output from the combustion chamber at an equivalence ratio of 1 and a thermal conductivity of 6.7 W/m·K. As shown in the figure, increasing the inlet flow velocity from 4 m/s to 16 m/s results in a continuous decrease in overall thermal efficiency, with values of 12.3%, 10. 6%, 9%, and 7.6%, respectively. The highest efficiency is achieved at the lowest velocity of 4 m/s, indicating that lower flow rates are more favorable for effective energy conversion under the studied conditions.

This reduction in efficiency with increasing velocity can be explained by several interacting factors. Although higher inlet velocities increase the mass flow rate and, consequently, the total rate of chemical energy supplied to the system (as described by Eq. (11)), they simultaneously reduce the residence time of the fluid within the combustion chamber. A shorter residence time limits the extent of chemical reactions, preventing complete combustion and leading to the formation of intermediate or unburned species such as CO and hydrocarbons. As a result, a portion of the available chemical energy is not fully converted into thermal energy, reducing the overall efficiency (as reflected in Eq. (12)).

In addition, higher flow velocities intensify convective heat transfer, which can enhance heat losses from the combustion chamber to the surroundings. Increased conduction through the walls and stronger convective transport within the fluid further contribute to the dissipation of thermal energy before it can be effectively utilized. These combined effects reduce the fraction of useful energy retained within the system, leading to a decline in overall thermal efficiency.

A similar decreasing trend is observed for radiative thermal efficiency. At lower inlet velocities, the flame temperature is relatively higher and the fluid remains longer within the high-temperature reaction zone, allowing radiating species such as CO_2 and H_2O sufficient time to emit thermal radiation. This results in a higher proportion of radiative heat transfer. However, as the inlet velocity increases, the reduction in both residence time and effective flame temperature weakens the radiation process. The conditions required for sustained emission from participating media are not fully achieved, and the contribution of radiative heat transfer to the total energy output decreases accordingly.

Table 1. Comparison between maximum total efficiencies reported for various micro combustors in the related studies.

Reference	Fuel	Combustor	η_{Total} (%)
Peng et al. [53]	H2	A micro combustor with backward facing step	1.14
Peng et al. [54]	H2/C3H8	A micro combustor with porous medium	2
Wei et al. [45]	H2/CH4	A micro combustor with block	2.2
Lee et al. [55]	H2/NH3	A heat-recirculating micro combustor	2.21
Jiang et al. [56]	H2	A micro combustor with baffle	2.83
Su et al. [57]	H2	A Multiple channel micro combustor	2.83†
Alipoor et al. [37]	H2	A radial micro combustor	3.14
Zuo et al. [58]	H2	A micro planar combustor	3.54
Bani et al. [59]	H2	A micro combustor with porous medium	4.37†
Akhtar et al. [60]	H2	Stepped micro combustors with different cross-sectional area	5.33
Alipoor & Saidi [5]	H2	A micro combustor including U-shaped microtube	6.3
Mohammadpour et al. [36]	H2/NH3	A radial micro combustor	8.2
Qian et al. [47]	H2	A micro combustor filled with inert porous medium and baffle	9.41
Present study	H2	Proposed micro-combustor	12.3

† Denotes that just radiation efficiency reported. The total efficiency is calculated by considering the amount of 15 % for MTPV efficiency
* All reported efficiency values correspond to the optimized configuration and operating conditions considered in each respective study.

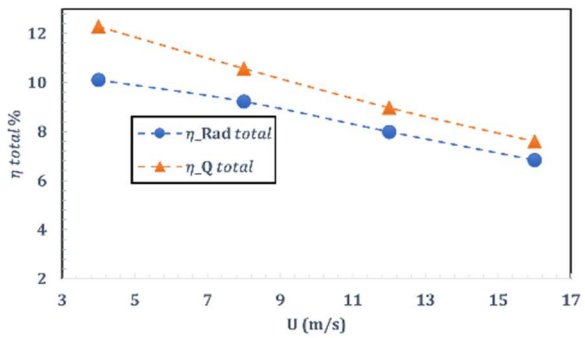


Fig. 16. Effect of different inlet velocity on total and radiant thermal efficiency, φ = 1 and λ_s = 6/7 W/m.K.

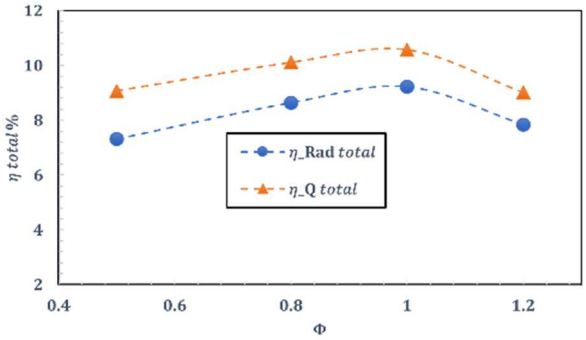


Fig. 17. Effect of different equivalence ratio on total and radiant thermal efficiency, U = 8 m/s and λ_s = 6/7 W/m.K.

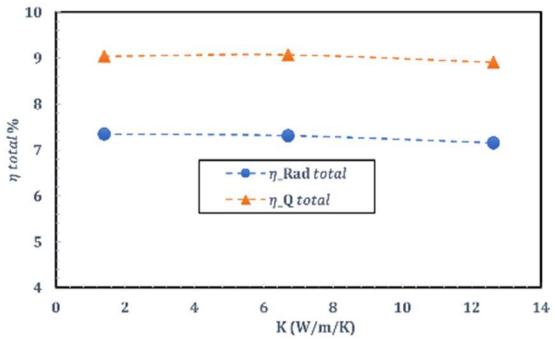


Fig. 18. Effect of different thermal conductivity coefficient on total and radiant thermal efficiency, U = 8 m/s and φ = 0.5.

Figure 17 presents the effect of equivalence ratio on overall and radiative thermal efficiency under conditions of U = 8 m/s and λ_s = 6.7 W/m·K. The results indicate that the overall thermal efficiency changes with equivalence ratio, reaching 9.06%, 10.1%, 10.6%, and 9.01%, with the highest value occurring at an equivalence ratio of unity. As the equivalence ratio increases, overall thermal efficiency rises toward stoichiometric conditions and decreases thereafter. In lean conditions (equivalence ratio less than one), the excess oxidizer causes a significant portion of the released energy to be used in heating inert gases, keeping the flame temperature low. Approaching the stoichiometric ratio, the fuel and oxidizer react more completely, converting the maximum amount of chemical energy into heat; therefore, overall thermal efficiency reaches its peak. In contrast, at equivalence ratios greater than one (rich mixtures), limited oxygen prevents complete combustion, and part of the fuel is converted to incomplete products. This reduces the useful energy released, leading to a decrease in overall thermal efficiency. In general, the maximum thermal efficiency occurs near stoichiometric conditions because fuel and oxidizer react completely, releasing the most chemical energy.

Figure 18 presents the influence of thermal conductivity on overall and radiative thermal efficiencies under conditions of U = 8 m/s and φ = 0.5. As shown in Fig. 18(a), the overall thermal efficiency corresponding to thermal conductivities of 1.4, 6.7, and 12.63 W/m·K is 9.03%, 9.06%, and 8.90%, respectively. This trend can be explained by the interaction of two competing heat transfer mechanisms within the system. On one hand, increasing thermal conductivity enhances heat recirculation through the solid walls, which improves preheating of the incoming fuel–air mixture. This leads to more favorable ignition conditions, more complete combustion, and a more uniform temperature distribution within the reaction zone. As a result, a larger fraction of the chemical energy is effectively converted into useful thermal energy, contributing to a slight increase in overall efficiency at moderate conductivity levels.

Table 1 summarizes the reported efficiency values of different micro-combustor configurations. The comparison is primarily based on overall thermal efficiency, because this parameter is more commonly reported in the literature and therefore provides a more consistent basis for comparing different micro-combustor systems. The previously reported overall efficiencies listed in Table 1 generally remain below 10%, with values ranging from approximately 1.14% to 9.41%. In comparison, the present micro-combustor achieves a maximum overall thermal efficiency of 12.3% under the investigated conditions. This result indicates the potential of the proposed configuration for efficient thermal-energy utilization. The radiative thermal efficiency presented in Figs. 16–18 further characterizes the thermal radiation available for TPV conversion and complements the overall-efficiency comparison.

4. Conclusion

A three-dimensional numerical investigation was conducted to evaluate hydrogen–air combustion and thermophotovoltaic performance in an MIT-inspired micro-combustor integrating curvature, expansion, and contraction within a single compact configuration. The principal findings are summarized as follows:

- Inlet velocity strongly affects flame position and thermal performance. Increasing the velocity from 4 to 16 m/s shifts the flame downstream and decreases the overall thermal efficiency from 12.3% to 7.6%. Higher velocity increases the maximum temperatures and OH concentration but reduces the residence time and preheating of the incoming mixture.
- The equivalence ratio provides a clear optimum near stoichiometric conditions for thermal performance. At 8 m/s and a wall thermal conductivity of 6.7 W/m·K, the overall thermal efficiency increases from 9.06% at $\varphi = 0.5$ to a maximum of 10.6% at $\varphi = 1.0$ and then decreases to 9.01% at $\varphi = 1.2$. The maximum fluid temperature reaches 1956 K at $\varphi = 1.2$, whereas the maximum OH mass fraction is obtained near stoichiometric conditions.
- Wall thermal conductivity primarily affects heat redistribution and flame stabilization rather than the bulk fluid temperature. Increasing the conductivity from 1.4 to 12.63 W/m·K promotes upstream heat recirculation and advances the flame position, while improving temperature uniformity. However, excessive heat conduction increases thermal losses and slightly reduces the overall efficiency, which varies from 9.03% to 9.06% and then 8.90% for the three conductivity levels.
- The dominant physical mechanisms are the competition between residence time and convective transport, heat recirculation and reactant preheating through the solid wall, and heat dissipation to the surroundings. These mechanisms jointly determine flame position, reaction intensity, temperature distribution, and thermal efficiency.
- The main contribution of the proposed combustor is its integrated heat-recirculation geometry, in which curvature, expansion, and contraction are combined without relying on multiple discrete internal flame-holding elements. This configuration provides internal heat recirculation and reactant preheating while offering a compact platform for controlling flame stability and thermal characteristics for micro-combustion and TPV applications.

Author Contributions

M.A. Attarian contributed to the Conceptualization, Methodology, Software development, Numerical simulations, Formal analysis, Data curation, Visualization, Writing – original draft; A. Alipoor contributed to the Supervision, Conceptualization, Methodology, Validation, Interpretation of results, Writing – review & editing, Project administration. All authors have read and approved the final version of the manuscript.

Acknowledgments

Not applicable.

Conflict of Interest

The authors declared no potential conflicts of interest concerning the research, authorship, and publication of this article.

Funding

The authors received no financial support for the research, authorship, and publication of this article.

Data Availability Statements

The datasets generated and/or analyzed during the current study are available from the corresponding author on reasonable request.

References

[1] Kang, Z., Shi, Z., Ye, J., Tian, X., Huang, Z., Wang, H., Wei, D., Peng, Q., Tu, Y., A Review of Micro Power System and Micro Combustion: Present Situation, Techniques and Prospects, *Energies*, 16, 2023, 3201.
[2] Nauman, M., Pan, J., Wang, Y., Li, F., Ojo, A.O., Raza, A., A Review of Recent Advancements in Micro Combustion Techniques to Enhance Flame Stability and Fuel Residence Time, *International Journal of Hydrogen Energy*, 49, 2024, 1165–1193.
[3] Maruta, K., Micro and Mesoscale Combustion, *Proceedings of the Combustion Institute*, 33, 2011, 125–150.
[4] Dias, D.M., Resende, P.R., Afonso, A.M., A Review on Micro-Combustion Flame Dynamics and Micro-Propulsion Systems, *Energies*, 17, 2024, 1327.
[5] Alipoor, A., Saidi, M.H., Numerical Study of Hydrogen-Air Combustion Characteristics in a Novel Micro-Thermophotovoltaic Power Generator, *Applied Energy*, 199, 2017, 382–399.
[6] Yang, X., He, Z., Zhao, L., Dong, S., Tan, H., Effect of Channel Diameter on the Combustion and Thermal Behavior of a Hydrogen/Air Premixed Flame in a Swirl Micro-Combustor, *Energies*, 12, 2019, 3821.
[7] Yang, X., Yang, W., Dong, S., Tan, H., Flame Stability Analysis of Premixed Hydrogen/Air Mixtures in a Swirl Micro-Combustor, *Energy*, 209, 2020, 118495.
[8] Zhang, Z., Wu, K., Yao, W., Yuen, R., Wang, J., Enhancement of Combustion Performance in a Microchannel: Synergistic Effects of Bluff-Body and Cavity, *Fuel*, 265, 2020, 116940.
[9] Fontana, E., Capeletto, C.A., Santos, V.G.S., Garbin, E., Cunha, M.M., Luz, L.F.L., Numerical Analysis of Heat Recuperation in Micro-Combustors Using Internal Recirculation, *Chemical Engineering Science*, 211, 2020, 115301.



[10] Abbaspour, P., Alipoor, A., Numerical Study of Combustion Characteristics and Oscillating Behaviors of Hydrogen–Air Combustion in Converging–Diverging Microtubes, *International Journal of Heat and Mass Transfer*, 159, 2020, 120127.
[11] Naeemi, S., Hashemi, S.A., A Numerical Study on the Blow-Off Limit of Premixed Hydrogen/Air Flames in a Cylindrical Micro-Combustor, *Proceedings of the Institution of Mechanical Engineers, Part G: Journal of Aerospace Engineering*, 235, 2021, 1260–1273.
[12] Gao, W., Yan, Y., Huang, L., Zhang, W., Shen, K., Numerical Investigation on Combustion Characteristics of Premixed Hydrogen/Air in a Swirl Micro Combustor with Twisted Vanes, *International Journal of Hydrogen Energy*, 46, 2021, 40105–40119.
[13] Resende, P.R., Morais, L.C., Pinho, C., Afonso, A.M., Combustion Characteristics of Premixed Hydrogen/Air in an Undulate Microchannel, *Energies*, 15, 2022, 626.
[14] Gao, W., Yan, Y., Shen, K., Huang, L., Zhao, T., Gao, B., Combustion Characteristic of Premixed H2/Air in the Micro Cavity Combustor with Guide Vanes, *Energy*, 239, 2022, 121975.
[15] You, J., Yan, Y., He, Z., Xue, Z., Zhang, C., Chen, Y., Comprehensive Numerical Investigations on the Thermal Performance of Heat Recirculating Micro Combustor with Pin Fins for Micro-Thermal Voltaic System Applications, *International Journal of Hydrogen Energy*, 47, 2022, 38043–38054.
[16] Tang, S., Wei, J., Xie, B., Shi, Z., Wang, H., Tian, X., He, B., Peng, Q., Experimental and Numerical Investigation on H2-Fueled Thermophotovoltaic Micro Tube with Multi-Cavity, *Energy*, 274, 2023, 127325.
[17] Huang, Z., Peng, Q., Shi, Z., Fu, G., Xiao, H., Huang, C., Numerical and Experimental Investigation of H2/CH4/Air Combustion Characteristics and Thermal Performance in the Combustor with Multi-Bluff-Body, *Fuel*, 367, 2024, 131435.
[18] Abbaspour, P., Alipoor, A., Numerical Study of Wavy-Wall Effects on Premixed H2/Air Flammability Limits, Propagation Modes, and Thermal Performance of Micro Combustion Chambers, *Applied Energy*, 359, 2024, 122727.
[19] Sarrafan Sadeghi, S., Tabejamaat, S., Ghahremani, A., Narimani Asl, S., A Novel Swiss-Roll Counterflow Micro-Combustor: Experimental Investigation of Methane-Oxygen Flame Behavior over Time, *Applied Thermal Engineering*, 255, 2024, 123978.
[20] Zuo, W., Li, F., Li, Q., Chen, Z., Huang, Y., Chu, H., Multi-Objective Optimization of Micro Planar Combustor with Tube Outlet by RSM and NSGA-II for Thermophotovoltaic Applications, *Energy*, 291, 2024, 130396.
[21] Zuo, W., Wang, Z., Li, Q., Zhou, K., Huang, Y., Numerical Investigations on the Performance Enhancement of a Hydrogen-Fueled Micro Planar Combustor with Finned Bluff Body for Thermophotovoltaic Applications, *Energy*, 293, 2024, 130752.
[22] Dai, C., Zuo, W., Li, Q., Zhou, K., Huang, Y., Zhang, G., E, J., Energy Conversion Efficiency Improvement Studies on the Hydrogen-Fueled Micro Planar Combustor with Multi-Baffles for Thermophotovoltaic Applications, *Energy*, 313, 2024, 134099.
[23] Dai, C., Zuo, W., Li, Q., Zhou, K., Huang, Y., Zhang, G., E, J., Numerical Investigations on the Performance of a Hydrogen-Fueled Micro Planar Combustor with V-Shaped Baffle for Thermophotovoltaic Applications, *Energy*, 326, 2025, 136270.
[24] Tenkolu, G.A., Gao, L., Tang, A., Cai, T., Zhang, H., Liu, C., Flame Stability Enhancement and Output Performance Optimization of a Dual Reaction Zone Recirculating Micro-Combustor, *Applied Thermal Engineering*, 258, 2025, 124559.
[25] Wan, J., Fan, A., Effect of Solid Material on the Blow-Off Limit of CH4/Air Flames in a Micro Combustor with a Plate Flame Holder and Preheating Channels, *Energy Conversion and Management*, 101, 2015, 552–560.
[26] Wan, J., Fan, A., Yao, H., Effect of the Length of a Plate Flame Holder on Flame Blowout Limit in a Micro-Combustor with Preheating Channels, *Combustion and Flame*, 170, 2016, 53–62.
[27] Fan, A., Zhang, H., Wan, J., Numerical Investigation on Flame Blow-Off Limit of a Novel Microscale Swiss-Roll Combustor with a Bluff-Body, *Energy*, 123, 2017, 252–259.
[28] Wang, S., Yuan, Z., Fan, A., Experimental Investigation on Non-Premixed CH4/Air Combustion in a Novel Miniature Swiss-Roll Combustor, *Chemical Engineering and Processing: Process Intensification*, 139, 2019, 44–50.
[29] Wan, J., Fan, A., Recent Progress in Flame Stabilization Technologies for Combustion-Based Micro Energy and Power Systems, *Fuel*, 286, 2021, 119391.
[30] Li, J., Yang, G., Wang, S., Fan, A., Experimental and Numerical Investigation on Non-Premixed CH4/Air Combustion in a Micro Swiss-Roll Combustor, *Fuel*, 349, 2023, 128740.
[31] Wang, S., Li, J., Fan, A., Effects of Channel Height on the Combustion Efficiency and Thermal Performances of a Micro Swiss-Roll Combustor, *Applied Thermal Engineering*, 238, 2024, 121956.
[32] Lv, E., Wang, S., Fan, A., Combustion Performances of a Novel Micro-Combustor with a Backward Facing Step and an Exhaust Gas Recirculation Channel, *Applied Thermal Engineering*, 246, 2024, 122929.
[33] Mohammadi, H., Alipoor, A., Investigation of Flame Structure, Emissions, and Thermal Behavior of Hydrogen–Ammonia Combustion in a Swiss-Roll Microcombustor, *Energy Conversion and Management: X*, 31, 2026, 102140.
[34] Mohammadi, H., Alipoor, A., Numerical Study on the Effect of Modular Structures on Hydrogen-Air Combustion for Micro Thermophotovoltaic Applications, *Energy*, 336, 2025, 138565.
[35] Alipoor, A., Abbaspour, P., Characteristic of Premixed Hydrogen/Air Tubular Flames in Microcombustor: Effects of Stimulated and Unstimulated Inlet Conditions on Flame Dynamics, *International Journal of Energy Research*, 2024, 2024, 3819821.
[36] Mohammadpour, A., Mazaheri, K., Alipoor, A., Mohammadpour, M., Effect of Oxidizer Dilution on Thermophotovoltaic Performance of Premixed Ammonia/Hydrogen/Air Combustion in Radial Micro-Combustor, *Fuel*, 331, 2023, 125874.
[37] Alipoor, A., Kadkhoda, A., Abbaspour, P., Combustion Characteristics of Hydrogen-Air Mixture in a Radial Micro Combustor for Using in Thermophotovoltaic Devices, *International Journal of Energy Research*, 45, 2021, 13616–13635.
[38] Burke, M.P., Chaos, M., Ju, Y., Dryer, F.L., Klippenstein, S.J., Comprehensive H2/O2 Kinetic Model for High-Pressure Combustion, *International Journal of Chemical Kinetics*, 44, 2012, 444–474.
[39] Kuo, C.H., Ronney, P.D., Numerical Modeling of Non-Adiabatic Heat-Recirculating Combustors, *Proceedings of the Combustion Institute*, 31, 2007, 3277–3284.
[40] Chen, C.-H., Ronney, P.D., Three-Dimensional Effects in Counterflow Heat-Recirculating Combustors, *Proceedings of the Combustion Institute*, 33, 2011, 3285–3291.
[41] Fan, A., Zhang, H., Wan, J., Numerical Investigation on Flame Blow-Off Limit of a Novel Microscale Swiss-Roll Combustor with a Bluff-Body, *Energy*, 123, 2017, 252–259.
[42] Zuo, W., E, J., Lin, R., Numerical Investigations on an Improved Counterflow Double-Channel Micro Combustor Fueled with Hydrogen for Enhancing Thermal Performance, *Energy Conversion and Management*, 159, 2018, 163–174.
[43] Yilmaz, H., Cam, O., Tangoz, S., Yilmaz, I., Effect of Different Turbulence Models on Combustion and Emission Characteristics of Hydrogen/Air Flames, *International Journal of Hydrogen Energy*, 42, 2017, 25744–25755.
[44] Wan, J., Fan, A., Maruta, K., Yao, H., Liu, W., Experimental and Numerical Investigation on Combustion Characteristics of Premixed Hydrogen/Air Flame in a Micro-Combustor with a Bluff Body, *International Journal of Hydrogen Energy*, 37, 2012, 19190–19197.
[45] Wei, D., Peng, Q., Wang, H., Tian, X., Xiao, H., Liu, H., Fu, G., Experimental Investigation of Blended H2/CH4 Combustion in Combustors with Block for Micro-Thermophotovoltaic, *Fuel*, 357, 2024, 129869.
[46] Yang, X., Zhao, L., He, Z., Dong, S., Tan, H., Comparative Study of Combustion and Thermal Performance in a Swirling Micro Combustor under Premixed and Non-Premixed Modes, *Applied Thermal Engineering*, 160, 2019, 114110.
[47] Qian, P., Liu, M., Li, X., Xie, F., Huang, Z., Luo, C., Zhu, X., Effects of Bluff-Body on the Thermal Performance of Micro Thermophotovoltaic System Based on Porous Media Combustion, *Applied Thermal Engineering*, 174, 2020, 115281.
[48] Yang, X., He, Z., Cha, S., Zhao, L., Dong, S., Tan, H., Parametric Analysis on the Combustion and Thermal Performance of a Swirl Micro-Combustor for Micro Thermophotovoltaic System, *Energy*, 198, 2020, 117312.
[49] Yang, X., He, Z., Zhao, L., Dong, S., Tan, H., Effect of Channel Diameter on the Combustion and Thermal Behavior of a Hydrogen/Air Premixed Flame in a Swirl Micro-Combustor, *Energies*, 12, 2019, 3821.
[50] Mansouri, Z., Combustion in Wavy Micro-Channels for Thermo-Photovoltaic Applications – Part I: Effects of Wavy Wall Geometry, Wall Temperature Profile and Reaction Mechanism, *Energy Conversion and Management*, 198, 2019, 111155.
[51] Zhang, Y., Pan, J., Tang, A.K., Lu, Q., Zha, Z., Bani, S., Effects of Inlet Parameters on Combustion Characteristics of Premixed CH4/Air in Micro Channels, *Journal of the Energy Institute*, 92, 2019, 824–834.

[52] Amani, E., Alizadeh, P., Moghadam, R.S., Micro-Combustor Performance Enhancement by Hydrogen Addition in a Combined Baffle-Bluff Configuration, *International Journal of Hydrogen Energy*, 43, 2018, 8127–8138.
[53] Peng, Q., E, J., Yang, W.M., Xu, H., Chen, J., Zhang, F., Meng, T., Qiu, R., Experimental and Numerical Investigation of a Micro-Thermophotovoltaic System with Different Backward-Facing Steps and Wall Thicknesses, *Energy*, 173, 2019, 540–547.
[54] Peng, Q., Yang, W., E, J., Li, Z., Xu, H., Fu, G., Li, S., Investigation on H2/Air Combustion with C3H8 Addition in the Combustor with Part/Full Porous Medium, *Energy Conversion and Management*, 228, 2021, 113652.
[55] Lee, S.I., Um, D.H., Kwon, O.C., Performance of a Micro-Thermophotovoltaic Power System Using an Ammonia-Hydrogen Blend-Fueled Micro-Emitter, *International Journal of Hydrogen Energy*, 38, 2013, 9330–9342.
[56] Jiang, D., Yang, W., Chua, K.J., Ouyang, J., Thermal Performance of Micro-Combustors with Baffles for Thermophotovoltaic System, *Applied Thermal Engineering*, 61, 2013, 670–677.
[57] Su, Y., Cheng, Q., Song, J., Si, M., Numerical Study on a Multiple-Channel Micro Combustor for a Micro-Thermophotovoltaic System, *Energy Conversion and Management*, 120, 2016, 197–205.
[58] Zuo, W., Wang, Z., E, J., Li, Q., Cheng, Q., Wu, Y., Zhou, K., Numerical Investigations on the Performance of a Hydrogen-Fueled Micro Planar Combustor with Tube Outlet for Thermophotovoltaic Applications, *Energy*, 263, 2023, 125957.
[59] Bani, S., Pan, J., Tang, A., Lu, Q., Zhang, Y., Micro Combustion in a Porous Media for Thermophotovoltaic Power Generation, *Applied Thermal Engineering*, 129, 2018, 596–605.
[60] Akhtar, S., Kurnia, J.C., Shamim, T., A Three-Dimensional Computational Model of H2–Air Premixed Combustion in Non-Circular Micro-Channels for a Thermo-Photovoltaic (TPV) Application, *Applied Energy*, 152, 2015, 47–57.

ORCID iD

Alireza Alipoor https://orcid.org/0000-0003-0523-8344

© 2026 Shahid Chamran University of Ahvaz, Ahvaz, Iran. This article is an open access article distributed under the terms and conditions of the Creative Commons Attribution-NonCommercial 4.0 International (CC BY-NC 4.0 license) (http://creativecommons.org/licenses/by-nc/4.0/).

How to cite this article: Attarian M.A., Alipoor A. Numerical Study of Heat Recirculation on Combustion Performance and Thermal Efficiency in a Novel Hydrogen–Air Micro-Combustor, *J. Appl. Comput. Mech.*, xx(x), 2026, 1–17. https://doi.org/10.22055/jacm.2026.49538.6058

Publisher's Note Shahid Chamran University of Ahvaz remains neutral with regard to jurisdictional claims in published maps and institutional affiliations.